

# Advances in Biomimetic Photoelectrocatalytic Reduction of Carbon Dioxide

Shaohan Xu, Qi Shen, Jingui Zheng, Zhiming Wang, Xun Pan, Nianjun Yang,\*  
and Guohua Zhao\*

Emerging photoelectrocatalysis (PEC) systems synergize the advantages of electrocatalysis (EC) and photocatalysis (PC) and are considered a green and efficient approach to CO<sub>2</sub> conversion. However, improving the selectivity and conversion rate remains a major challenge. Strategies mimicking natural photosynthesis provide a prospective way to convert CO<sub>2</sub> with high efficiency. Herein, several typical strategies are described for constructing biomimetic photoelectric functional interfaces; such interfaces include metal cocatalysts/semiconductors, small molecules/semiconductors, molecular catalysts/semiconductors, MOFs/semiconductors, and microorganisms/semiconductors. The biomimetic PEC interface must have enhanced CO<sub>2</sub> adsorption capacity, preferentially activate CO<sub>2</sub>, and have an efficient conversion ability; with these properties, it can activate C=O bonds effectively and promote electron transfer and C–C coupling to convert CO<sub>2</sub> to single-carbon or multicarbon products. Interfacial electron transfer and proton coupling on the biomimetic PEC interface are also discussed to clarify the mechanism of CO<sub>2</sub> reduction. Finally, the existing challenges and perspectives for biomimetic photoelectrocatalytic CO<sub>2</sub> reduction are presented.

## 1. Introduction

As a notorious greenhouse gas and a potential carbon feedstock, the transformation of carbon dioxide (CO<sub>2</sub>) into high value-added fuels or chemicals has been recognized as a promising way to mitigate energy shortages and problems caused by the greenhouse effect.<sup>[1]</sup> Nevertheless, CO<sub>2</sub> reduction is faced with several challenges. The solubility of CO<sub>2</sub> in water under ambient temperature and pressure conditions is only 0.033 M,<sup>[2]</sup> so it underperforms when competing with H<sub>2</sub>O molecules during the adsorption process. The low solubility and diffusion rate of CO<sub>2</sub> in aqueous solution greatly restricts the efficiency of CO<sub>2</sub> conversion. In addition, CO<sub>2</sub> is a nonpolar linear molecule with two strong  $\pi_3^4$  bonds; these bonds cause the energy of the C=O bond (750 kJ mol<sup>-1</sup>)<sup>[3]</sup> to be significantly higher than that of the C–H bond and C–C bond. An immense amount of energy is


required to break the C=O bonds owing to the molecular structure, which contributes to the relatively low conversion rate.<sup>[4]</sup> In addition, the carbon atom in CO<sub>2</sub> is in its highest oxidation state, which allows the CO<sub>2</sub> reduction reaction (CO<sub>2</sub>RR) to go through various multielectron transfer processes, leading to poor product selectivity.<sup>[5]</sup> Therefore, methods of enhancing the conversion rate and product selectivity of the CO<sub>2</sub>RR must be investigated.

Natural photosynthesis in green plants is an efficient process in which atmospheric CO<sub>2</sub> and H<sub>2</sub>O molecules are converted to glucose and oxygen through a moderate and efficient pathway via enzyme catalysis, sustaining the carbon-oxygen cycle on Earth.<sup>[6]</sup> It has been found that plant leaves have a perfect 3D hierarchical porous structure with high porosity, high connectivity, and a high specific surface area.<sup>[7]</sup> These structures are not only conducive to the adsorption of sunlight but also favor the efficient migration of materials such as CO<sub>2</sub> and H<sub>2</sub>O for photosynthesis and transpiration. Natural photosynthesis consists of two processes: light reactions and dark reactions (Figure 1a). Atmospheric carbon dioxide and water first enter the interior of the leaves through the stomata on the surface of the leaves. In the light reaction, chlorophyll, the reaction center, harvests photons to generate electron-hole pairs. The water is oxidized to oxygen by the photogenerated holes, providing electrons and protons for the fixation of CO<sub>2</sub>.<sup>[8]</sup> Subsequently, in the dark reaction, CO<sub>2</sub> is captured, activated and converted via a cyclic and directed electron

S. Xu, Q. Shen, J. Zheng, Z. Wang, X. Pan, G. Zhao  
School of Chemical Science and Engineering  
Key Laboratory of Spine and Spinal Cord Injury Repair and Regeneration,  
Ministry of Education, Tongji Hospital  
Tongji University  
Shanghai 200092, China  
E-mail: g.zhao@tongji.edu.cn

N. Yang  
Institute of Materials Engineering  
University of Siegen  
57076 Siegen, Germany  
E-mail: nianjun.yang@uni-siegen.de

Q. Shen  
Institute of New Energy, School of Chemistry and Chemical Engineering  
Shaoxing University  
508 Huancheng West Road, Shaoxing, Zhejiang 312000, China

 The ORCID identification number(s) for the author(s) of this article can be found under <https://doi.org/10.1002/advs.202203941>

© 2022 The Authors. Advanced Science published by Wiley-VCH GmbH. This is an open access article under the terms of the Creative Commons Attribution License, which permits use, distribution and reproduction in any medium, provided the original work is properly cited.

DOI: 10.1002/advs.202203941

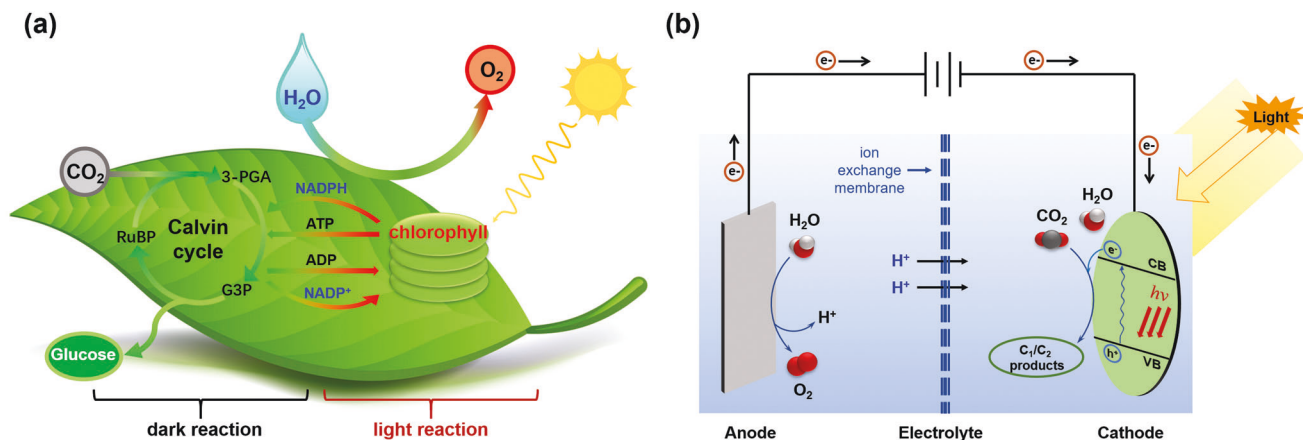


Figure 1. Schematics of a) natural photosynthesis and b) PEC CO<sub>2</sub> reduction.

transfer process, the Calvin cycle. The enzyme ribulose biphosphate carboxylase/oxygenase (RuBisCO) enables CO<sub>2</sub> to combine with ribulose 1,5-bisphosphate (RuBP) to yield a six-carbon compound, achieving the activation of CO<sub>2</sub> molecules. This six-carbon compound is extremely unstable and rapidly decomposes into two three-carbon molecules, 3-phosphoglycerate (3-PGA). 3-PGA is reduced by the NADPH produced from the light reaction, undergoes a series of complex proton-coupled electron transfer (PCET) processes and is eventually converted to glucose.<sup>[9]</sup>

Inspired by natural photosynthesis, the photocatalytic reduction of CO<sub>2</sub> mimicking the light reaction has been developed since the 1970s.<sup>[10]</sup> Photocatalysis (PC) is considered a promising technique for CO<sub>2</sub> reduction owing to the moderate reaction conditions and lack of extra energy input.<sup>[11]</sup> However, PC still faces several problems, such as the uncontrollability of electron transfer, which results in the poor selectivity of the reduction products, the easy recombination of photogenerated electrons and holes,<sup>[5]</sup> and the susceptibility of semiconductors to photocorrosion.<sup>[12]</sup> Directed electron transfer, which can be achieved in the dark reaction in natural photosynthesis, is difficult to achieve through PC because the photocatalytic interface is a heterogeneous interface where the photogeneration of electrons is not cyclic; the photogenerated electrons are gradually consumed as the PC reaction proceeds. In contrast, electrocatalysis (EC) has the merits of strong controllability, since an electrochemical system is a closed and cyclic system where the electrons can move directionally upon application of an external voltage. In addition, protons can be generated at the anode and subsequently migrate to the cathode to participate in CO<sub>2</sub> reduction. However, the EC process usually requires large amounts of electrical energy input owing to the high overpotentials of the CO<sub>2</sub>RR. Therefore, biomimetic PEC, which integrates PC and EC, can complement each other and achieve the thorough imitation of photosynthesis, providing a multiproton and multielectron cyclic coupling reaction mode (Figure 1b). The electrons can be produced from the light reaction, and directed electron transfer can be implemented by tuning the applied voltages, which mimics the dark reaction in photosynthesis. The applied potentials can effectively inhibit the recombination of photogenerated electrons and holes, enhancing the photocatalytic efficiency. Furthermore, solar energy can supply additional charge, lowering electricity consumption.<sup>[13]</sup> The

advantages and disadvantages of PC, EC, and PEC for CO<sub>2</sub> reduction are listed in Table 1.

In addition to efficient photoelectron transfer and recycling, the reduction of CO<sub>2</sub> in the dark reaction, which involves recyclable electron/proton transfer and CO<sub>2</sub> adsorption, activation and conversion, is also notable. The preliminary step of the CO<sub>2</sub> conversion process in natural photosynthesis is the adsorption of CO<sub>2</sub> molecules. The leaves of green plants, which have a perfect 3D porous structure with high porosity, connectivity, and specific surface area, can efficiently transfer CO<sub>2</sub> to the chloroplast stroma to complete photosynthesis through their stomata. The ultrahigh specific areas provide many active sites for CO<sub>2</sub> adsorption. The porous structure is favorable for the mass transport of CO<sub>2</sub> and H<sub>2</sub>O,<sup>[14]</sup> and the light loss can be reduced owing to the reflection of incident light in porous structures.<sup>[15]</sup> After the efficient transport and adsorption of CO<sub>2</sub>, the rapid activation of C=O bonds can be achieved by the RuBisCO enzyme. Following a series of complex electron transfer and proton coupling processes, the selective conversion of CO<sub>2</sub> to glucose is accomplished. Moreover, during the fixation of CO<sub>2</sub> in photosynthesis, the indispensable proton transferase NADPH is formed by the reduction and protonation of the electron acceptor NADP<sup>+</sup> in the light reaction.<sup>[16]</sup> The cyclic redox reaction between NADP<sup>+</sup> and NADPH can supply recyclable protons and electrons for the CO<sub>2</sub>RR. Analogous to natural photosynthesis, a remarkable biomimetic PEC interface could adsorb, fix, and activate CO<sub>2</sub> and recycle electrons and protons.

Unlike several excellent previous reviews focusing on the catalysts,<sup>[5,17]</sup> catalytic methods,<sup>[18]</sup> and products<sup>[19]</sup> of CO<sub>2</sub> reduction, also those related to photoelectrocatalytic CO<sub>2</sub> conversion which focuses on the functions and performance of a specific category of catalytic materials or the selection of semiconductors,<sup>[20]</sup> strategies for selective CO<sub>2</sub> conversion to different products,<sup>[21]</sup> and reaction mechanisms,<sup>[22]</sup> our review sheds light on strategies for constructing a biomimetic PEC interface to realize certain functions of photosynthesis, focusing on one or several factors to simulate natural processes. Most recently, a review focusing on structural design of artificial leaves has been published in which the concept of mimicking natural photosynthesis is introduced in terms of catalyst design resembling the structure and function of plant leaves.<sup>[6]</sup> In this context, we redefine the PEC CO<sub>2</sub> reduction

**Table 1.** List of advantages and disadvantages of PC, EC and PEC for CO<sub>2</sub> reduction.

Type of catalytic methods	Advantages	Disadvantages
PC	<ul style="list-style-type: none"> <li>Moderate reaction conditions</li> <li>Energy saving</li> </ul>	<ul style="list-style-type: none"> <li>Easy recombination of photogenerated electrons and holes</li> <li>Susceptibility of semiconductors to photocorrosion</li> <li>Uncontrollability of electron transfer resulting in the poor product selectivity</li> </ul>
EC	<ul style="list-style-type: none"> <li>Strong controllability achieved by closed and cyclic electrochemical systems</li> <li>Feasible integration with other technologies</li> <li>Easy to operate</li> </ul>	<ul style="list-style-type: none"> <li>High electrical energy consumption</li> <li>Decreased stability due to electrode passivation</li> </ul>
PEC	<ul style="list-style-type: none"> <li>Suppression of the recombination of photogenerated electron–hole pairs</li> <li>Lower electricity consumption</li> <li>High efficiency</li> </ul>	<ul style="list-style-type: none"> <li>Relatively complex operation and equipment</li> <li>Further investigations required for the reaction mechanisms of PEC CO<sub>2</sub> reduction</li> </ul>

system as a simulation of natural photosynthesis. The process by which a semiconductor is excited by illumination to produce photogenerated electron–hole pairs mimics the light reaction of photosynthesis. The directed electron transfer induced by the applied electric field mimics the dark reaction, which realizes the controllability of the electron transfer process by regulating the applied voltage. In this review, we propose several strategies for constructing an effective biomimetic PEC interface consisting of a metal cocatalyst/semiconductor, small molecule/semiconductor, molecular catalyst/semiconductor, MOF/semiconductor and microorganism/semiconductor. Enhanced CO<sub>2</sub> adsorption capacity, effective CO<sub>2</sub> activation and efficient conversion are essential for a remarkable biomimetic PEC interface so that the C=O bonds can be activated efficiently and electron transfer and proton coupling can occur. To better understand the underlying reaction mechanisms, the interfacial electron transfer process on different biomimetic PEC interfaces and possible reaction pathways involving proton coupling are elucidated. To this end, the existing challenges and future development of biomimetic PEC interfaces for CO<sub>2</sub> reduction will be discussed and outlined.

## 2. Construction of Biomimetic Photoelectrocatalytic Interfaces

An excellent biomimetic PEC interface must exhibit prominent light absorption capacity, rapid photoelectric separation efficiency, high specific area for CO<sub>2</sub> adsorption and abundant reactive sites for effective activation of CO<sub>2</sub>. Thus far, individual catalytic components do not yet meet all of the above requirements. The components have several limitations, such as inadequate contact between CO<sub>2</sub> and the catalytic interface, poor carbon fixation performance, a substantial activation energy barrier, and unspecific product selectivity. Therefore, the effective assembly of catalysts with different functions is needed to complement the advantages of each. Building biomimetic PEC interfaces to achieve effective CO<sub>2</sub> capture and fixation on one interface is a promising research direction. In this section, we aim to review different strategies for the construction of biomimetic PEC interfaces. These interfaces can be categorized as metal cocatalysts/semiconductors, small molecules/semiconductors, molec-

ular catalysts/semiconductors, MOFs/semiconductors, and microorganisms/semiconductors (Table 2).

### 2.1. Metal Cocatalyst/Semiconductor Biomimetic Interfaces

The incorporation of cocatalysts cannot only favor the rapid separation of photogenerated electron–hole pairs but also accelerate sluggish reaction kinetics by lowering the overpotential of the CO<sub>2</sub>RR. The additional active sites provided by the metal cocatalyst can also facilitate the activation of the absorbed CO<sub>2</sub> molecules. Cocatalysts with specific functions can be used to adjust the adsorption strength of certain intermediates, promoting the selectivity for the desired products.<sup>[23]</sup> In addition, the side or back reactions can be suppressed by cocatalysts to further improve the product selectivity.<sup>[24]</sup> Accordingly, cocatalyst deposition can be considered an effective way to enhance the activation and selective reduction of CO<sub>2</sub>.

Metals such as Au, Ag, Pd, Cu, and Pt are among the most prevalent cocatalysts employed in PC and PEC CO<sub>2</sub> reduction. The combination of a metal and a semiconductor can suppress the recombination of photogenerated electrons and holes. For example, deposition of 10 wt% Cu nanoparticles (NPs) on graphene oxide can suppress the recombination of charge carriers by enhancing charge separation at the metal/semiconductor interface and achieve the efficient activation of CO<sub>2</sub> through single-electron transfer from the d orbital of the metal to the  $\pi^*$  orbital of C–O, increasing the yield of photocatalytic CO<sub>2</sub> to methanol by nearly 60 times.<sup>[25]</sup> The deposition of metal can also alter the light absorption range and enhance light absorption. For instance, TiO<sub>2</sub> films modified by Au NPs can widen the light absorption range of TiO<sub>2</sub> to the visible spectrum and increase the methane yield by 24 times.<sup>[26]</sup> The broadening of TiO<sub>2</sub> light absorption range might be attributed to the localized surface plasmon resonance (LSPR) effect of Au NPs, which is derived from the collective oscillations of the electrons in the vicinity of the plasmonic nanostructure induced by the incident light.<sup>[27]</sup> Due to this effect, noble metal NPs can absorb visible light and inject the photoinduced electrons into the conduction band of semiconductor to produce the visible light responsive TiO<sub>2</sub>.<sup>[28]</sup> In addition

**Table 2.** List of several biomimetic photoelectrocatalytic interfaces for CO<sub>2</sub> reduction.

Composition	Biomimetic functional interface							Refs.
	Major products	Number of electrons transferred	Selectivity [%]	FE [%]	TON	Yield [μmol/g-cat/h]	Quantum yield [%]	
<b>Metal cocatalyst/semiconductor</b>								
Pt/TiO <sub>2</sub>	CH <sub>4</sub>	8	N.A.	N.A.	N.A.	1361	2.41	[29]
Au-Cu/P25	CH <sub>4</sub>	8	97	N.A.	N.A.	2200	N.A.	[38]
Cu@TiO <sub>2</sub> -Au	HCOOH	2	98	82.6	N.A.	N.A.	N.A.	[39]
Au-Cu/SrTiO <sub>3</sub> /TiO <sub>2</sub>	CO	2	N.A.	N.A.	N.A.	3770	N.A.	[40]
Au-Pd/TiO <sub>2</sub> {101}	CH <sub>4</sub>	8	71	N.A.	N.A.	N.A.	N.A.	[41]
Rh LWS/TiO <sub>2</sub>	C <sub>2</sub> H <sub>5</sub> OH	12	N.A.	N.A.	N.A.	12.1	N.A.	[92a]
Au-ZnTe/ZnO	CO	2	66.0	63.0	N.A.	N.A.	N.A.	[92b]
Pd/TiO <sub>2</sub>	CO, CH <sub>4</sub>	2, 8	10.1, 69.2	N.A.	N.A.	22.2, 38.1	N.A.	[92c]
<b>Small molecule/semiconductor</b>								
NH <sub>3</sub> /g-C <sub>3</sub> N <sub>4</sub>	CH <sub>4</sub> , CH <sub>3</sub> OH	8, 6	N.A.	N.A.	N.A.	1.39, 1.87	N.A.	[47]
NH <sub>2</sub> -C/Cu <sub>2</sub> O	HCOOH	2	92	N.A.	N.A.	138.65	N.A.	[48]
Amine-functionalized graphene/CdS	CH <sub>4</sub>	8	N.A.	N.A.	N.A.	2.84	N.A.	[93a]
Amine/g-C <sub>3</sub> N <sub>4</sub>	CH <sub>4</sub> , CH <sub>3</sub> OH	8, 6	N.A.	N.A.	N.A.	0.34, 0.28	N.A.	[93b]
<b>Molecular catalyst/semiconductor</b>								
[Ru-dcbpy]/N-Ta <sub>2</sub> O <sub>5</sub>	HCOOH	2	75	N.A.	89	N.A.	1.9	[56]
Ru(bpy) <sub>2</sub> dppz/Co <sub>3</sub> O <sub>4</sub>	HCOO <sup>-</sup>	2	99.95	86	N.A.	N.A.	N.A.	[57]
[Ru-dpbpy]/N-Ta <sub>2</sub> O <sub>5</sub> anchored by PO <sub>3</sub> H <sub>2</sub>	HCOOH	2	N.A.	N.A.	118	N.A.	N.A.	[58]
CoTPP/g-C <sub>3</sub> N <sub>4</sub>	HCOOH	2	100	N.A.	137	N.A.	N.A.	[64]
Coqpy@mesoporous graphitic C <sub>3</sub> N <sub>4</sub>	CO	2	98	N.A.	128	N.A.	0.25	[94b]
Re complex/CuInS <sub>2</sub> /NiO	CO	2	N.A.	32	11	N.A.	N.A.	[94c]
<b>MOF/semiconductor</b>								
ZIF8/Zn <sub>2</sub> GeO <sub>4</sub>	CH <sub>3</sub> OH	6	N.A.	N.A.	N.A.	0.22	N.A.	[71]
Cu <sub>3</sub> (BTC) <sub>2</sub> /TiO <sub>2</sub>	CH <sub>4</sub>	8	N.A.	N.A.	N.A.	2.64	N.A.	[72]
Co-ZIF9/g-C <sub>3</sub> N <sub>4</sub>	CO	2	86.3	N.A.	N.A.	495	0.9	[73]
Ni <sub>3</sub> (HITP) <sub>2</sub> /[Ru(bpy) <sub>3</sub> ] <sup>2+</sup>	CO	2	97	N.A.	N.A.	34 500	N.A.	[95a]
Ni(II) MOF/g-C <sub>3</sub> N <sub>4</sub>	CO, CH <sub>4</sub>	2, 8	N.A.	N.A.	N.A.	13.6	N.A.	[95b]
CTU/TiO <sub>2</sub>	CO	2	N.A.	N.A.	N.A.	31.32	N.A.	[95c]
UiO-66/MoS <sub>2</sub>	CH <sub>3</sub> COOH	8	94	N.A.	N.A.	39.0	N.A.	[95d]
<b>Microorganism/semiconductor</b>								
<i>Sporomusa ovata</i> /Si nanowire	CH <sub>3</sub> COOH	8	N.A.	90	N.A.	N.A.	N.A.	[84]
<i>Methanosarcina barkeri</i> /n <sup>+</sup> /p-Si/NiMo	CH <sub>4</sub>	8	N.A.	82	N.A.	N.A.	N.A.	[86]
<i>Moorella thermoacetica</i> /AuNCs	CH <sub>3</sub> COOH	8	N.A.	N.A.	N.A.	34.76	2.86	[96a]

to the incorporation of versatile metals with semiconductors, the performance of metal/semiconductor hybrid catalytic interfaces is governed by the particle sizes of the metal cocatalysts. For example, an investigation of the influence of Pt NPs with different sizes on the photocatalytic performance of TiO<sub>2</sub> showed that as the size of the Pt particles decreases, the work function of Pt shifts from the bottom of the VB of TiO<sub>2</sub> to the CB and vacuum energy level, as shown in **Figure 2a**.<sup>[29]</sup> With the decrease in the size of Pt NPs (0.5–2 nm) and the work function, the maximum separation rate of electron-hole pairs can be reached; in this study, the optimal photocatalytic performance was obtained. However, further decreases in the size of the Pt NPs can lead to a work function that is higher than the CB, which suppresses the transfer of electrons.

In addition to the size of metal NPs, the facet also plays an essential role in the performance of metal–semiconductor hybrid

catalysts. Bai et al.<sup>[30]</sup> investigated the facet selectivity of Pd cocatalysts in graphitic-phase C<sub>3</sub>N<sub>4</sub> (g-C<sub>3</sub>N<sub>4</sub>) nanosheets and revealed that Pd{111} facets favored the reduction of CO<sub>2</sub> more than Pd{100} facets. The theoretical results showed that the adsorption energy of CO<sub>2</sub> in the presence of Pd{111} ( $E_a = 0.230$  eV) is much higher than that with Pd{100} ( $E_a = 0.064$  eV), demonstrating a better performance for CO<sub>2</sub> adsorption on Pd{111}. In addition, the activation energy barriers of CO<sub>2</sub> reduction can be lowered by the participation of Pd{111} facets within the range of 7.15 to 3.98 eV. Therefore, due to the merits of g-C<sub>3</sub>N<sub>4</sub>, CO<sub>2</sub> reduction can be favorable in the case of Pd{111} facets.

Bimetallic cocatalysts have attracted much attention because they can tune the surface adsorption energy of CO<sub>2</sub> and improve the product selectivity because they combine the properties of different metals to achieve a synergistic effect. Different metals

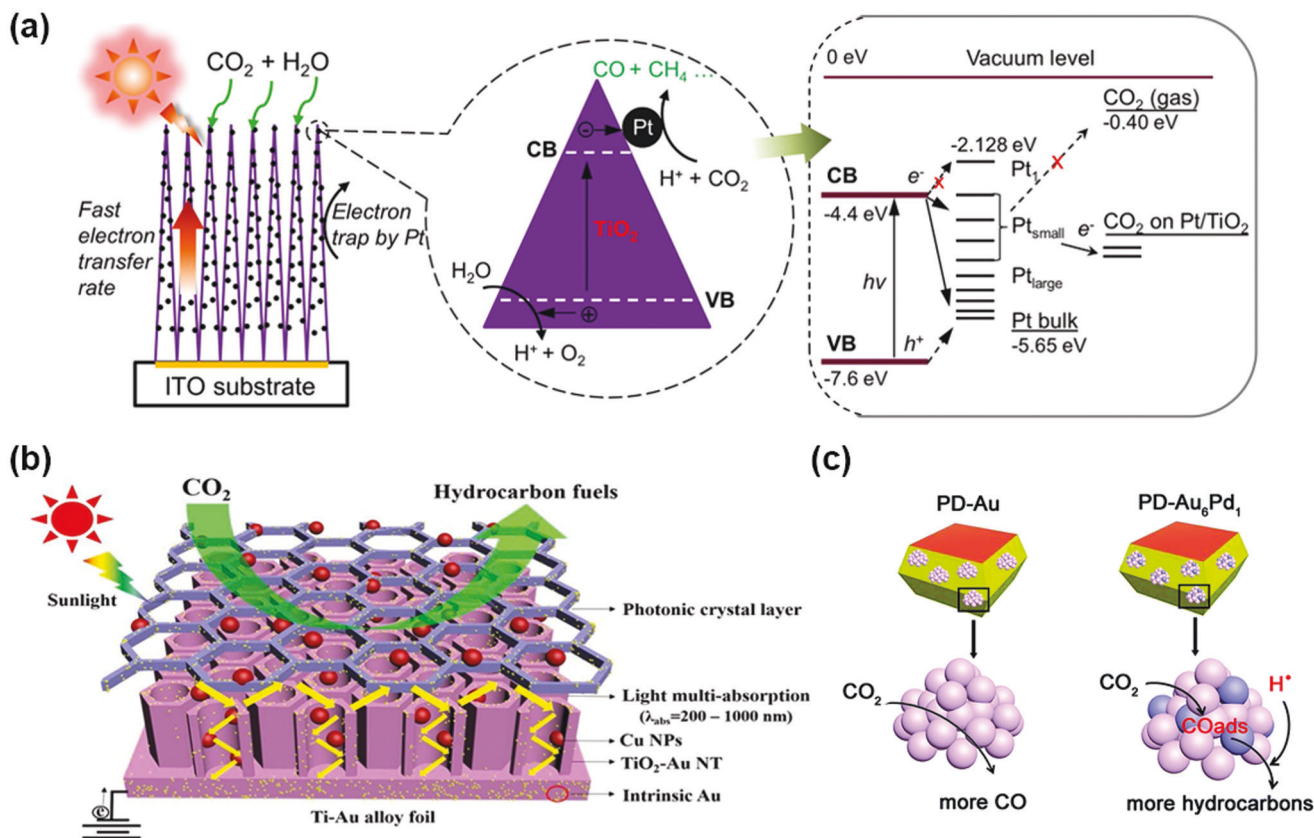


**Figure 2.** a) Schematic diagram of CO<sub>2</sub> photoreduction mechanism by using Pt–TiO<sub>2</sub> nanostructured films. Reproduced with permission.<sup>[29]</sup> Copyright 2012, American Chemical Society. b) Schematic diagram for the synergy of the photonic crystal, Au NPs, and Cu NPs for CO<sub>2</sub> reduction under light illumination. Reproduced with permission.<sup>[39]</sup> Copyright 2017, Elsevier. c) A schematic illustration of the product distribution on PD–Au and PD–Au<sub>6</sub>Pd<sub>1</sub>. Reproduced with permission.<sup>[41]</sup> Copyright 2019, Royal Society of Chemistry.

show different adsorption capacities for \*CO<sub>2</sub><sup>•-</sup>, \*CO, \*HCO, and other intermediates in the CO<sub>2</sub> reduction process, leading to various CO<sub>2</sub> reduction products. Typically, Au, Ag, and Zn weakly adsorb the CO<sub>2</sub> activation intermediate \*CO, and thus, the main reduction product is CO. The weak adsorption capacity of Sn, Hg, and Pb for \*CO<sub>2</sub><sup>•-</sup> is favorable to the production of formic acid.<sup>[31]</sup> With respect to Cu, the Cu–C bond strength when the intermediate \*CO is adsorbed is moderate, favoring the conversion of CO<sub>2</sub> to multielectron and multicarbon compounds.<sup>[32]</sup> Therefore, the product selectivity of the CO<sub>2</sub>RR can be controlled by adjusting the ratio of metals with different functions in the design of metal alloy cocatalysts.

Bimetallic cocatalysts such as Ni–Ga,<sup>[33]</sup> Cu–Ag,<sup>[34]</sup> Cu–Au,<sup>[35]</sup> Cu–Pd,<sup>[36]</sup> and Mo–Bi<sup>[37]</sup> exhibit a more remarkable CO<sub>2</sub> electrocatalysis performance than single-metal catalysts, as they integrate multiple functional components to achieve a synergistic effect. P25 decorated with Au–Cu NPs showed a better CO<sub>2</sub> photocatalysis performance than Au/P25 and Cu/P25.<sup>[38]</sup> The yield of methane on Au–Cu/P25 (2200 μmol g<sup>-1</sup> h<sup>-1</sup>) was much higher than that on single-metal decorated Au/P25 (210 μmol g<sup>-1</sup> h<sup>-1</sup>) and Cu/P25 (280 μmol g<sup>-1</sup> h<sup>-1</sup>). Au and Cu play different roles in the photocatalytic system; the LSPR effect of Au broadens the response range of materials to visible light, while Cu can achieve the specific adsorption of the reaction intermediate CO. Another example is the decoration of Cu NPs and Au NPs on TiO<sub>2</sub> nan-

otube photonic crystals (NTPC), which leads to a 1019.3 μmol L<sup>-1</sup> cm<sup>-2</sup> formic acid yield in 8 h, almost 6.3 times higher than that on traditional TiO<sub>2</sub> NTs (Figure 2b).<sup>[39]</sup> During catalysis, the local surface plasmon resonance effect of the intrinsic Au NPs promotes the utilization of visible light at the catalytic interface. TiO<sub>2</sub> NTPC can not only act as a light harvester but also provide a large specific area for the deposition of Cu NPs. Cu NPs also act as reactive sites and synergistically facilitate PEC CO<sub>2</sub> reduction. The product selectivity can be further improved by tuning the composition of the bimetallic cocatalysts. For instance, Kang et al.<sup>[40]</sup> analyzed the CO<sub>2</sub> photocatalytic performance of different proportions of Au–Cu alloy-modified SrTiO<sub>3</sub>/TiO<sub>2</sub> nanotube arrays (STO/TiO<sub>2</sub> NTAs). The main product of Au@STO/TiO<sub>2</sub> NTAs for the reduction of CO<sub>2</sub> was CO due to the weak adsorption capacity of Au for the intermediate CO. With the incorporation of Cu NPs, the selectivity of CO<sub>2</sub>RR to CO decreased, and the selectivity to hydrocarbons increased. Among them, Au<sub>3</sub>Cu@STO/TiO<sub>2</sub> NTAs showed the best activity for reducing CO<sub>2</sub> to hydrocarbons, and the performance was significantly better than that of the non-alloy system (Au<sub>3</sub>+Cu<sub>1</sub>@STO/TiO<sub>2</sub>).

In addition to the incorporation of Au–Cu bimetallic cocatalysts, a Au–Pd alloy decorated on TiO<sub>2</sub>{101} facets was fabricated to enhance the conversion of CO<sub>2</sub> to hydrocarbons (Figure 2c).<sup>[41]</sup> The Au–Pd alloy can provide copious CO<sub>2</sub> adsorption and activation sites with dispersed Pd atoms acting as

hydrogenation centers. The cooperative combination of the Au–Pd alloy and the semiconductor TiO<sub>2</sub> contributes to efficient CO<sub>2</sub> reduction. Different elemental compositions of the Au–Pd alloy cocatalysts were explored for their photocatalytic CO<sub>2</sub> reduction performance. Pd–Au<sub>6</sub>Pd<sub>1</sub> exhibited optimal CO<sub>2</sub> conversion reactivity with a maximum hydrocarbon selectivity of 85%. To determine the reasons for the excellent performance of Pd–Au<sub>6</sub>Pd<sub>1</sub>, further investigations were conducted. Pd–Au<sub>6</sub>Pd<sub>1</sub> exhibited a significantly higher CO<sub>2</sub> adsorption ability, and an obvious LSPR absorption peak corresponding to Au was revealed by UV–vis diffuse reflectance spectroscopy. The presence of SPR and the corresponding plasmonic heat effect facilitated the activation of CO<sub>2</sub> and lowered the energy barrier for the CO<sub>2</sub>RR.

Metal cocatalysts can effectively broaden the photoresponse range of semiconductors through localized surface plasmon resonance. The formation of a surface Schottky energy barrier can lead to the accumulation of photogenerated electrons on cocatalysts, facilitating the separation of photoexcited carriers.<sup>[42]</sup> Moreover, the incorporation of metal cocatalysts can supply abundant active sites for both CO<sub>2</sub> adsorption and activation, reducing the reaction energy barrier for CO<sub>2</sub> reduction. For some cocatalysts with unique functions, the side reactions can be suppressed, and thus, the selectivity of the desired product can be enhanced. Nevertheless, factors such as the particle size and facet of metal NPs and composition and proportion of bimetallic cocatalysts should be taken into consideration when selecting and loading the cocatalysts, as these factors affect the performance of the catalyst and the product selectivity of the CO<sub>2</sub>RR.

## 2.2. Small Molecule/Semiconductor Biomimetic Interfaces

Despite the nonpolar linear structure of CO<sub>2</sub> molecules, the surface charge distribution leads to positively charged C atoms and negatively charged O atoms, indicating the presence of both Lewis acid centers and Lewis base centers on the surface of the CO<sub>2</sub> molecules.<sup>[43]</sup> Hence, modification of the catalytic surface with acidic or basic molecules can improve the fixation and activation of CO<sub>2</sub>.

Carbon dots (CDs), a carbon nanomaterial with various functional groups, can provide active sites for highly selective catalysis and linking groups to form connections with other materials.<sup>[44]</sup> Cu–CD nanocorals synthesized by decorating carbon dots on Cu were reported to improve the adsorption of CO<sub>2</sub> and reduce CO<sub>2</sub> to formic acid at a low overpotential (0.13 V) with a 79% (–0.7 V versus RHE) total Faradaic efficiency (FE) (Figure 3a).<sup>[45]</sup> The Fourier transform infrared (FT-IR) spectrum and XPS results demonstrated that the carbon dot modification provided abundant functional groups, such as –OH, –NH–, and –C=O, on the surface of the Cu nanocorals. These functional groups enhanced the adsorption capacity of CO<sub>2</sub> by 3.4 times (0.22 mmol g<sup>–1</sup> at 25 °C) and improved the adsorption of H<sup>+</sup>. The concentrations of CO<sub>2</sub> and H<sup>+</sup> played a pivotal role in the PCET mechanism of CO<sub>2</sub> reduction; thus, the increase in both concentrations on the catalyst surface directly led to the excellent CO<sub>2</sub> catalytic performance of the Cu–CD nanocorals.

Amino acids are small molecules that can improve the stability of CO<sub>2</sub> reduction intermediates on the catalytic interface. In one study, the reduction of CO<sub>2</sub> was performed on Cu electrodes

modified with different amino acids, which increased the hydrocarbon production selectivity on the Cu electrode.<sup>[46]</sup> The results showed that all the tested amino acids enhanced the selectivity of CO<sub>2</sub> to hydrocarbons, while different amino acids exhibited different abilities to increase the product selectivity. For example, modification with glycine maximized the selectivity of the CO<sub>2</sub>RR (Figure 3b). Theoretical investigations showed that modification with amino acids can facilitate the formation of hydrogen bonds between CO<sub>2</sub> and –NH<sub>3</sub><sup>+</sup> in amino acid molecules, thereby stabilizing the two most important intermediates, COOH\* and CHO\*, in the conversion of CO<sub>2</sub> to hydrocarbons.

An amine modification strategy can be employed to suppress the hydrogen evolution reaction (HER) and enhance the product selectivity of the CO<sub>2</sub>RR. One example focused on modifying and functionalizing the surface of g-C<sub>3</sub>N<sub>4</sub> with NH<sub>3</sub> to obtain a hierarchical nanosheet that exhibited an enhanced light harvesting ability, abundant reactive sites, increased CO<sub>2</sub> adsorption and improved separation of charge carriers.<sup>[47]</sup> The N<sub>2</sub> adsorption-desorption isotherms showed that amine-functionalized C<sub>3</sub>N<sub>4</sub> nanosheets showed a much higher adsorption capacity than pristine C<sub>3</sub>N<sub>4</sub> due to the presence of mesopores. The assembly of ultrathin C<sub>3</sub>N<sub>4</sub> nanosheets led to the formation of an interconnected porous structure, which increased the specific area and facilitated mass transport. Amine decoration can enhance the CO<sub>2</sub> adsorption ability via acid–base interactions between CO<sub>2</sub> and the amine. Another study reported a threefold improvement in HCOOH yield on Cu<sub>2</sub>O functionalized with amino groups (Figure 3c).<sup>[48]</sup> The enhancement can be attributed to both the strong chemisorption of CO<sub>2</sub> by the interaction between the CO<sub>2</sub> (acid) and –NH<sub>2</sub> (base) and the suppression of the competing HER. In addition, as an electron acceptor, amino acids can accelerate charge transfer on the catalyst surface, inhibiting the recombination of photogenerated electrons and holes. The remarkable auxiliary function of the amine can also be verified on the EC interface. An example is the investigation of electrochemical CO<sub>2</sub> reduction activity on Ag nanoparticle surfaces capped with oleylamine, oleic acid, and dodecanethiol.<sup>[49]</sup> The results revealed that decoration with amines and thiols can both enhance the adsorption of CO<sub>2</sub> to lead to the formation of a strong –COOH bond. However, modifications with thiols can also lead to a strong interaction with protons, which also strengthens the HER. Compared with thiol-capped Ag NPs, the amine-capped Ag surface destabilizes hydrogen binding, which suppresses the HER. Therefore, modifications with amines improved the CO production selectivity of the Ag nanoparticles (Figure 3d). The Faradaic efficiency of the CO<sub>2</sub> to CO conversion on oleylamine-capped Ag reached 94.2%, which was higher than that on oleic acid-capped Ag (89.1%) and dodecanethiol-capped Ag (65.5%).

Alkali metals are other small molecules that can be used to decorate semiconductors. They not only facilitate the activation of CO<sub>2</sub> but also promote the separation of photogenerated electrons and holes to overcome one of the predominant shortcomings of semiconductors. For instance, KOH can be decorated on C<sub>3</sub>N<sub>4</sub> to improve its performance for photocatalytic CO<sub>2</sub> reduction (Figure 3e).<sup>[50]</sup> The measurement of the CO<sub>2</sub> reduction performance on C<sub>3</sub>N<sub>4</sub> modified by KOH, KCl, K<sub>2</sub>CO<sub>3</sub>, and KHCO<sub>3</sub> indicated that K<sup>+</sup> alone cannot promote the reaction. In a comparison of the product yield of the CO<sub>2</sub>RR on C<sub>3</sub>N<sub>4</sub> modified with different

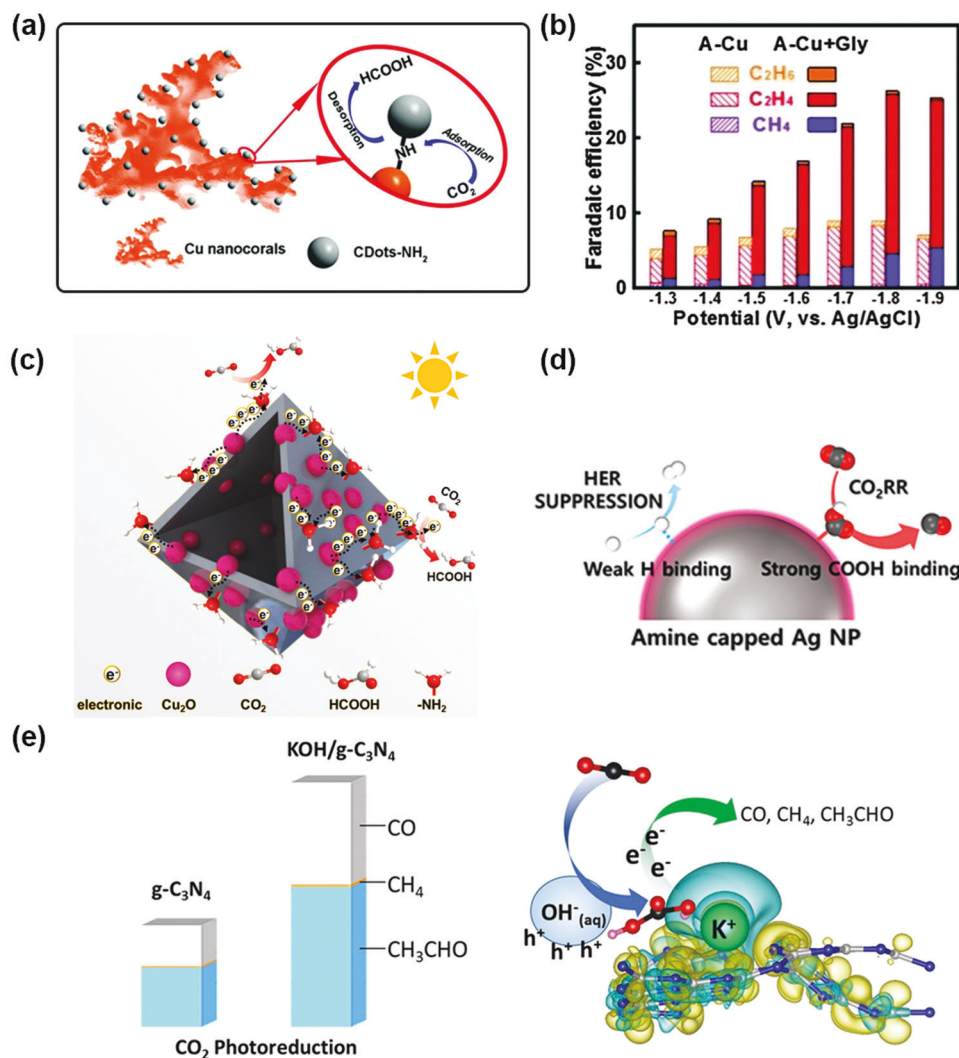


**Figure 3.** a) The proposed reaction mechanism of electrocatalytic CO<sub>2</sub> reduction by Cu-CDots nanocorals. Reproduced with permission.<sup>[45]</sup> Copyright 2017, Royal Society of Chemistry. b) Electrochemical CO<sub>2</sub> reduction on bare and glycine-modified annealed Cu electrodes in the full potential range from -1.3 to -1.9 V. Reproduced with permission.<sup>[46]</sup> Copyright 2016, Royal Society of Chemistry. c) Schematic illustration the process of charge migration and the proposed photocatalytic reduction of CO<sub>2</sub> to HCOOH via the NH<sub>2</sub>-C@Cu<sub>2</sub>O catalyst. Adapted with permission.<sup>[48]</sup> Copyright 2021, Elsevier. d) Schematic of the HER and CO<sub>2</sub>RR process on Amine capped Ag NP. Reproduced with permission.<sup>[49]</sup> Copyright 2017, American Chemical Society. e) The performance and effect of KOH decorated photoelectrode. Reproduced with permission.<sup>[50]</sup> Copyright 2017, Elsevier.

concentrations of NaOH and KOH, the results showed that the yields of CO and CH<sub>4</sub> on C<sub>3</sub>N<sub>4</sub> decorated with KOH was 1.5 times that on C<sub>3</sub>N<sub>4</sub> decorated with NaOH, indicating that the cations also influence the alkali metal-decorated photocatalyst. The results of the photocurrent density experiments of g-C<sub>3</sub>N<sub>4</sub> in Na<sub>2</sub>SO<sub>4</sub> solutions with different pH values illustrated that OH<sup>-</sup> can act as a hole acceptor to receive photogenerated holes and impede the recombination of photoexcited carriers. Theoretical calculation results show that although the adsorption energy of CO<sub>2</sub> on K<sup>+</sup> and Na<sup>+</sup>-modified g-C<sub>3</sub>N<sub>4</sub> did not improve over that of the original g-C<sub>3</sub>N<sub>4</sub> (0.25 eV), the adsorption of H<sub>2</sub>CO<sub>3</sub> on K/g-C<sub>3</sub>N<sub>4</sub> (1.13 eV) was 31% higher than that on Na/g-C<sub>3</sub>N<sub>4</sub> (0.86 eV). This result was ascribed to the position of K<sup>+</sup> on the g-C<sub>3</sub>N<sub>4</sub>; it tended to be located outside the pores, which was favorable for the adsorption of H<sub>2</sub>CO<sub>3</sub>. The stronger adsorption of H<sub>2</sub>CO<sub>3</sub> may lead

to the better photocatalytic performance of CN with KOH modification than with NaOH modification.

Small molecules employed for modifying the surface of semiconductors usually contain functional groups such as -OH and -NH-. These molecules all possess electron donors, which can provide adsorption sites for the electrophilic carbon atoms in CO<sub>2</sub> and H<sup>+</sup> from the electrolyte to activate and convert CO<sub>2</sub>.

### 2.3. Molecular Catalyst/Semiconductor Biomimetic Interfaces

In natural photosynthesis, chlorophyll, a magnesium porphyrin derivative, can harvest light and transform solar energy with porphyrin as the core photosensitive component.<sup>[51]</sup> Mimicking the structure of chlorophyll, numerous researchers have dedicated

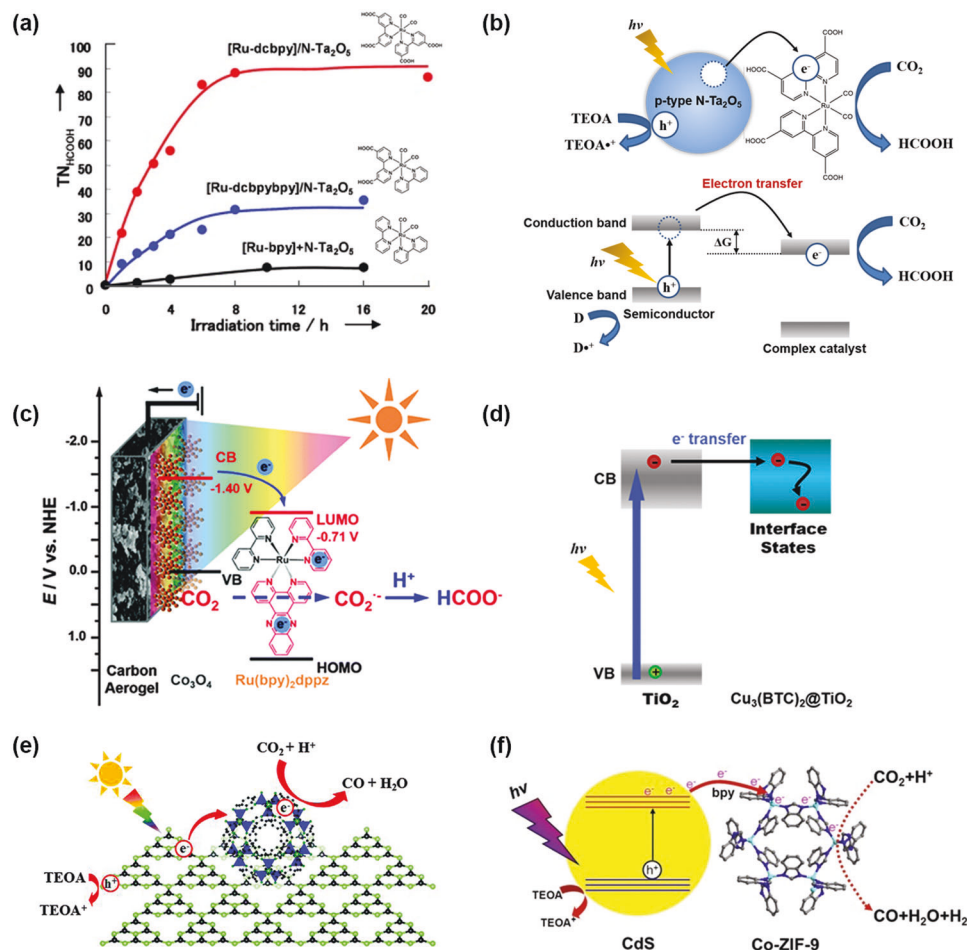


**Figure 4.** a) Turnover number for HCOOH formation from CO<sub>2</sub> as a function of irradiation time on N-Ta<sub>2</sub>O<sub>5</sub> with different Ru complexes decorated in CO<sub>2</sub>-saturated MeCN/TEOA (5:1) solution and b) energy diagram of hybrid photocatalysis under visible light with a semiconductor and a metal complex. Adapted with permission.<sup>[56]</sup> Copyright 2010, Wiley-VCH. c) Schematic plots of the CO<sub>2</sub> adsorption-enhanced Ru(bpy)<sub>2</sub>dppz-Co<sub>3</sub>O<sub>4</sub>/CA interface together with its energy level diagram and the possible reaction pathways for CO<sub>2</sub> conversion on this photocathode. Such a PEC interface is composed of CA as the CO<sub>2</sub>-adsorption substrate, Ru(bpy)<sub>2</sub>dppz as the molecular catalyst, and Co<sub>3</sub>O<sub>4</sub> as the photoelectrocatalyst. Reproduced with permission.<sup>[57]</sup> Copyright 2016, Royal Society of Chemistry. d) Schematic illustration of the involved electron behavior. Reproduced with permission.<sup>[72]</sup> Copyright 2014, Wiley-VCH. e) The schematic diagrams of photocatalytic CO<sub>2</sub> reduction on Co-ZIF9/g-C<sub>3</sub>N<sub>4</sub>. Reproduced with permission.<sup>[73]</sup> Copyright 2014, Royal Society of Chemistry. f) The schematic diagrams of photocatalytic CO<sub>2</sub> reduction on Co-ZIF9/CdS. Reproduced with permission.<sup>[74]</sup> Copyright 2015, Elsevier.

their efforts to the development of molecular catalysts composed of various metal centers, especially transition metals, and ligands for CO<sub>2</sub> reduction. Central multivalence transition metals in metal complexes can act as redox centers, which favors the implementation of multielectron transfer processes in the CO<sub>2</sub>RR.<sup>[17b]</sup> Reaction intermediates can form via interactions between the metal centers and CO<sub>2</sub> molecules, facilitating the reduction of CO<sub>2</sub>. Molecular catalysts can be roughly divided into four categories based on their ligands: 1) macrocyclic ligand metal catalysts, whose central metals are typically Co, Fe, Ni, and Cu;<sup>[52]</sup> 2) bipyridine ligand metal complexes (Re, Ru, Mn, etc.);<sup>[53]</sup> 3) phosphine ligand metal complexes (Rh, Pd);<sup>[54]</sup> and 4) biomimetic metal complexes (Fe<sub>4</sub>S<sub>4</sub> clusters).<sup>[55]</sup> Molecular catalysts for the CO<sub>2</sub>RR typically possess the advantages of high product selectivity; thus, decorating them on the surface of semiconductors can further enhance the selectivity of the CO<sub>2</sub>RR. In addition, molec-

ular catalysts can also act as photosensitizers to broaden the light response range of semiconductors.

Among the aforementioned ligands, macrocyclic ligands (porphyrin, phthalocyanine, cyclam, etc.) and bipyridine ligands are the two predominant ligands investigated by researchers. One of the earliest examples is a series of Ru complexes ([Ru-bpy], [Ru-dcbpybpy] and [Ru-dcbpy]) decorated on p-type semiconductor N-doped Ta<sub>2</sub>O<sub>5</sub> to selectively reduce CO<sub>2</sub> to formic acid under visible light in acetonitrile and triethanolamine solutions.<sup>[56]</sup> **Figure 4a** shows the TON<sub>HCOOH</sub> of CO<sub>2</sub> reduction on N-Ta<sub>2</sub>O<sub>5</sub> loaded with different Ru complexes in CO<sub>2</sub>-saturated acetonitrile/TEOA solution over time. The experiment found that after decoration with the Ru complex, the TON of formic acid produced from the CO<sub>2</sub>RR catalyzed by N-Ta<sub>2</sub>O<sub>5</sub> was significantly enhanced. The [Ru-dcbpy]/N-Ta<sub>2</sub>O<sub>5</sub> catalyst exhibited a selectivity of 75% for formic acid under 405 nm light, with a TON<sub>HCOOH</sub>



of 89 and a quantum efficiency of 1.9%. Photocatalytic CO<sub>2</sub>RR driven by the excitation of semiconductors by light to generate electrons that subsequently transfer from the conduction band to the ground state of the molecular catalysts was reported for the first time. The schematic diagram is shown in Figure 4b. The energy difference  $\Delta G$  between the bottom of the semiconductor conduction band and the reduction potential of CO<sub>2</sub> on the catalyst is an essential factor in photocatalytic CO<sub>2</sub> reduction.  $\Delta G$  can be optimized by changing the type of semiconductor, center atom, or ligand, thereby improving the photoactivity, selectivity, and stability of the catalyst. Adsorption capacity of the substrate is another important factor to be considered for the construction of efficient PEC interfaces. An example is a biomimetic interface for CO<sub>2</sub> reaction integrating the light harvester Co<sub>3</sub>O<sub>4</sub> and a ruthenium complex on the surface of a porous carbon aerogel, which has a high specific surface area (Figure 4c).<sup>[57]</sup> Carbon aerogel and the enzyme-mimicking ruthenium complex synergistically enhanced the concentration of surface-adsorbed CO<sub>2</sub>. The Co<sub>3</sub>O<sub>4</sub>/ruthenium complex composite catalyst effectively absorbed light and produced electrons under light irradiation. The photoinduced electrons rapidly underwent directed transfer to CO<sub>2</sub> in the electric field. CO<sub>2</sub> accepted the electrons and then underwent a two-electron reduction process, which selectively converted it to formic acid. It was shown that this CO<sub>2</sub> adsorption-enhanced biomimetic catalytic system had several advantages, including low energy consumption (the CO<sub>2</sub> reduction potential is only -0.45 V vs NHE), concentrated target product (formic acid selectivity >99%), and highly efficient conversion (Faradaic efficiency of 86%).

In addition, the connection between the semiconductor and the supporting molecules is also crucial for increasing the reaction rate. The immobilization of molecular catalysts on semiconductors in the aforementioned studies was realized by physical adsorption. The relatively feeble van der Waals interactions between molecular catalysts and semiconductors may lead to the leaching of catalysts, impairing the catalytic performance during long-term PEC.<sup>[17b]</sup> In addition, linkage via adsorption may reduce the efficiency of electron transfer between the metal complex and semiconductor. To achieve a strong linkage, phosphonate self-assembly was employed to bind the semiconductor N-Ta<sub>2</sub>O<sub>5</sub> and [Ru-dcbpy] to convert CO<sub>2</sub> into formic acid under visible light.<sup>[58]</sup> Different linking groups, including COOH and PO<sub>3</sub>H<sub>2</sub>, as well as different connection methods (anchoring with organic groups, physical adsorption and direct mixing), were investigated experimentally. The results showed that the main product on these four photocatalysts in the MeCN/TEOA (5:1, V/V) solution saturated with CO<sub>2</sub> was HCOOH, and the two-electron reduction product CO was also detected. Among them, the PO<sub>3</sub>H<sub>2</sub>-linked catalyst exhibited the highest photocatalytic activity with a high TON<sub>HCOOH</sub> of 118. This result indicated that the composite method and the chemical structure of the linking group can affect the photocatalytic activity of the catalyst.

Since then, an increasing number of molecular catalyst/semiconductor hybrid catalysts linked with different organic groups, such as cobalt porphyrin/conductive diamond linked by azide alkyne rings,<sup>[59]</sup> carboxyl-linked Re(CO)<sub>3</sub>-Cl(dcbpy)/rutile TiO<sub>2</sub>{001},<sup>[60]</sup> phosphate-linked Ru(II) binuclear complexes/Ag/TaON,<sup>[61]</sup> graphite-conjugated *fac*-Re(1,10-phenanthroline)(CO)<sub>3</sub>Cl,<sup>[62]</sup> and Re(bipy)/TiO<sub>2</sub>/Cu<sub>2</sub>O,<sup>[63]</sup> have

been investigated for photo/electrocatalytic CO<sub>2</sub> reduction. This kind of valence-bonded molecular catalyst/semiconductor system exhibits a rapid electron transfer channel, which can improve the quantum efficiency, TON and TOF of the CO<sub>2</sub> reaction. To date, the most extensively investigated linking groups have been phosphoric acid groups, carboxyl groups and other oxygenic functional groups, which are beneficial for bonding with the metal on the semiconductor surface. However, the electron transfer efficiency of the systems containing these linking groups cannot outperform that of the systems with double bond and  $\pi$ - $\pi$  stacking as the linking method. Liu et al.<sup>[64]</sup> constructed a catalytic Co-porphyrin/g-C<sub>3</sub>N<sub>4</sub> composite CO<sub>2</sub> system by  $\pi$ - $\pi$  stacking and realized the efficient adsorption and reduction of CO<sub>2</sub> to the two-electron product formic acid. The quasi-3D structure of CoTPP provided pores that were slightly larger than CO<sub>2</sub> molecules, which is suitable for the biomimetic adsorption of CO<sub>2</sub>. The electron cloud distribution indicates that the Co atoms in CoTPP can interact with O atoms in CO<sub>2</sub> to activate CO<sub>2</sub>. The photoelectrochemical properties showed that CoTPP/g-C<sub>3</sub>N<sub>4</sub> exhibits excellent visible light absorption performance and PEC CO<sub>2</sub> reduction capability. The conjugated  $\pi$ - $\pi$  structure of CoTPP facilitates extending the visible light absorption range to approximately 700 nm, which is beneficial to the photoelectric reduction of CO<sub>2</sub>. Additionally, electrochemical studies have shown that it has good CO<sub>2</sub> catalytic activity. The results revealed that it possessed a quasi-3D structure similar to that of MOFs and a large specific surface area attributed to g-C<sub>3</sub>N<sub>4</sub>, which favored the adsorption and reduction of CO<sub>2</sub>. In an aqueous electrolyte, at a low applied potential of -0.6 V, the amount of formic acid produced by photoelectric CO<sub>2</sub> reduction for 8 hours can reach up to 154.4  $\mu$ mol, and the TON can reach 137.

Molecular catalysts exhibit great advantages owing to the high controllability of their catalytic properties that can be gained by tailoring their molecular structures. The valence change of the central transition metal provides active sites for CO<sub>2</sub> reduction. Combining molecular catalysts with semiconductor materials is a promising way to enhance the selectivity of the desired products, and the decoration of molecular catalysts can broaden the light response range of semiconductors as photosensitizers. Typically, electron transfer occurs inside hybrid catalysts; thus, determining how to achieve efficient, fast, and directed electron transfer between molecular catalysts and semiconductors is a compelling frontier for researchers. In addition, methods of tuning the molecular structures to achieve efficient and highly selective CO<sub>2</sub> reduction are also worth investigating.

#### 2.4. MOF/Semiconductor Biomimetic Interfaces

Metal organic frameworks (MOFs), a unique category of molecular catalysts, have attracted extensive attention due to their 3D porous structures. Generally, metal ions or clusters are used as connection nodes, and organic ligands support the construction of a 3D extension of space. After the emergence of zeolite and carbon nanotubes, MOFs have become an important new porous material with diverse structures and convenient design processes and are widely employed in catalysis, energy storage, and separation.<sup>[65]</sup> Because their structure is similar

to the hierarchical porous structure of plant leaves that enable efficient material migration and abundant adsorption sites for CO<sub>2</sub> molecules, MOFs have an excellent adsorption capacity for CO<sub>2</sub>,<sup>[65c,66]</sup> which can facilitate the further reduction of CO<sub>2</sub>. For example, a Cu-based HKUST-1 MOF supported on gas diffusion electrode (GDE) with high surface area was synthesized and employed in electrocatalytic CO<sub>2</sub> reduction, achieving a 15.9% FE and a 17 h stability due to the preservation of its local structure.<sup>[67]</sup> Furthermore, the comparison results with the other three different porous materials indicated that the unsaturated coordination sites exposed in the porous structure favor the conversion of CO<sub>2</sub> to alcohols. In addition to the high surface area and robust structure, it is feasible to control and tune the local chemical environment of the active site in MOF to enhance its catalytic activity. A cationic functional group was tethered at the proximal end of the Fe-porphyrin active site by postsynthetic modification to precisely tune the catalytic performance of a Fe-porphyrin-based MOF via electrostatic secondary-sphere interactions.<sup>[68]</sup> The selectivity of electrochemical reduction of CO<sub>2</sub> to CO was substantially enhanced to nearly 100% by immobilizing pendent positively charged groups. In situ Raman measurement revealed that the enhanced electrocatalytic performance was ascribed to the electrostatic stabilization of CO intermediates, boosting its desorption from the catalyst surface. Although MOFs are one category of promising materials for electrocatalytic CO<sub>2</sub> reduction owing to the designable structures and dispersed metal active sites, their poor conductivity limits the enhancement of current density and performance. Yi et al. synthesized a conjugated 2D conductive phthalocyanine-based MOF (NiPc-NiO<sub>4</sub>) nanosheets as highly efficient electrocatalysts for CO<sub>2</sub> conversion to CO.<sup>[69]</sup> NiPc-NiO<sub>4</sub> exhibits good conductivity due to the high d-π orbital overlap between the nickel node and the catechol, resulting in a nearly 100% CO selectivity and 34.5 mA cm<sup>-2</sup> CO partial current density. MOFs can also be used as photocatalysts because of their photoresponse property. Wang et al. prepared three stable and isostructural MOFs (MOF-Ni, MOF-Co, and MOF-Cu) for heterogeneous photocatalytic CO<sub>2</sub> reduction.<sup>[11b]</sup> Among them, MOF-Ni displayed a remarkable selectivity of 97.7% for CO products. However, MOFs themselves have relatively low charge transfer efficiency when excited by light. Photocatalytic systems using single MOF-based photocatalysts require the participation of a sacrificial electron donor.<sup>[70]</sup>

To enhance the limited charge transfer efficiency, thus far, several research groups have combined MOFs with semiconductors and utilized the light excitation ability of semiconductors and the CO<sub>2</sub> adsorption and activation capacity of MOFs to improve the efficiency of CO<sub>2</sub> reduction. For example, the amount of methanol generated by ZIF8/Zn<sub>2</sub>GeO<sub>4</sub> composite photocatalytic CO<sub>2</sub> reduction increased by 62% over that of pure Zn<sub>2</sub>GeO<sub>4</sub> nanorods.<sup>[71]</sup> Studies have shown that ZIF8 itself does not have photocatalytic activity for CO<sub>2</sub>, but it can effectively adsorb CO<sub>2</sub> in aqueous solution and enhance the concentration of CO<sub>2</sub> on the semiconductor surface. ZIF8 also broadens the photoresponse range of Zn<sub>2</sub>GeO<sub>4</sub>, thereby improving the photocatalytic CO<sub>2</sub> reduction performance. Li et al.<sup>[72]</sup> combined Cu<sub>3</sub>(BTC)<sub>2</sub>, which has CO<sub>2</sub> adsorption capacity, with semiconductor TiO<sub>2</sub> to prepare a Cu<sub>3</sub>(BTC)<sub>2</sub>@TiO<sub>2</sub> core-shell structure that can efficiently reduce CO<sub>2</sub> to methane via photocatalysis (Figure 4d). The conversion efficiency was 5 times as high as that catalyzed by pristine TiO<sub>2</sub>,

and the ratio of methane to hydrogen increased from 22.7% to nearly 100%. Ultrafast transient absorption spectroscopy showed that after Cu<sub>3</sub>(BTC)<sub>2</sub> was combined with semiconductor TiO<sub>2</sub>, the lifetime of photogenerated electron-hole pairs was effectively increased by more than 25 times. This result can be explained by the fact that after the combination, the photogenerated electrons can quickly migrate from TiO<sub>2</sub> to the Cu<sub>3</sub>(BTC)<sub>2</sub>@TiO<sub>2</sub> interface within 1 ps and participate in the reduction of CO<sub>2</sub>. ZIF9, another kind of ZIF that can catalyze CO<sub>2</sub> reduction, was combined with a semiconductor to prepare two composite materials, Co-ZIF9/g-C<sub>3</sub>N<sub>4</sub><sup>[73]</sup> and Co-ZIF9/CdS.<sup>[74]</sup> Studies have corroborated that after semiconductor photocatalysts are combined with ZIF9, the ZIF9 assists in promoting the separation of photoinduced electrons and holes generated on the semiconductors. It can also promote the adsorption, capture, and fixation of CO<sub>2</sub>. Under visible light excitation, the semiconductor photocatalyst was excited to form photoinduced electron-hole pairs. The photogenerated electrons then migrated to the CO<sub>2</sub> adsorption sites on the MOF and participated in the conversion of CO<sub>2</sub> to CO. A schematic diagram is shown in Figure 4e,f. By tuning the reaction conditions, such as solvent and temperature, the selectivity of CO<sub>2</sub> reduction to CO in acetonitrile solution at 20 °C reached 91.2%.

Due to their abundance in the earth's crust, low cost, and unique properties for stabilizing reaction intermediates and promoting C-C coupling, Cu-based catalysts in either Cu<sup>2+</sup> or Cu<sup>+</sup> form have been widely investigated for CO<sub>2</sub> reduction. For instance, a multi-shelled CuO microboxes electrocatalyst was constructed and achieved a FE of 51.3% owing to the approachability of catalytic active sites and enhanced adsorption of CO intermediates.<sup>[75]</sup> Compared with Cu and CuO, Cu<sub>2</sub>O NPs display a good performance for generating C<sub>2</sub>+ products probably because the existence of low-coordinated Cu<sup>+</sup> species on the surface can facilitate the C-C coupling.<sup>[76]</sup> For example, a 59% FE for the electroreduction of CO<sub>2</sub> to ethylene was achieved on Cu<sub>2</sub>O NPs enclosed with both {111} and {100} facets.<sup>[76b]</sup> The joint interface between two facets possesses strong adsorption capability of CO intermediates to promote C-C coupling and weaker adsorption ability of the generated C<sub>2</sub>H<sub>4</sub> to facilitate its desorption from the interface. As the p-type semiconductors, CuO and Cu<sub>2</sub>O possess relatively narrow band gaps and exhibit outstanding photocatalytic activity by visible light irradiation.<sup>[77]</sup> Reduced graphene oxide-CuO nanocomposites were prepared for photocatalytic CO<sub>2</sub> reduction to methanol with a yield of 1228 μmol g<sup>-1</sup>.<sup>[78]</sup> In another study, Cu<sub>2</sub>O nanocrystals were employed in photocatalytic reduction of CO<sub>2</sub>, producing methanol as the sole product with a 72% internal quantum yield and 10% solar-to-fuel efficiency.<sup>[79]</sup> The (110) facets of the prepared Cu<sub>2</sub>O nanocrystals are probably Cu terminated, which accounts for their high photocatalytic activity. However, bare copper oxides are susceptible to photocorrosion during photocatalysis or photoelectrocatalysis, resulting in reduced catalytic activity. The porous framework of MOFs can protect unstable semiconductors from photocorrosion. For instance, a core-shell structure with Cu<sub>3</sub>(BTC)<sub>2</sub> MOFs decorated on Cu<sub>2</sub>O nanowires was constructed to improve the photocatalytic activity for CO<sub>2</sub> reduction to CH<sub>4</sub>.<sup>[80]</sup> Encapsulation in MOFs can protect unstable Cu<sub>2</sub>O from photocorrosion, and the semiconductor can enhance the light absorption capacity of the MOFs. With the combination of Cu-based MOFs, the yield of CH<sub>4</sub> can reach approximately 0.73 μmol for 8 h, which is

1.9 times higher than that of pristine  $\text{Cu}_2\text{O}$ . The reusability of the catalysts was investigated, and it was found that the incorporation of MOFs led to a higher catalytic stability and prolonged durability. In addition, the porous structure attributed to the MOFs increased the surface-to-volume ratio, which enhanced the  $\text{CO}_2$  adsorption capacity. The EIS results indicated that the hybrid catalyst possessed a lower charge transfer resistance than bare  $\text{Cu}_2\text{O}$ , demonstrating a faster charge transfer at the interface.

MOFs materials have a unique spatial 3D porous structure analogous to that of plant leaves, and this structure provides sufficient adsorption sites for molecules and high connectivity. By changing the central metal atom, tuning and modifying ligands and applying other manipulation methods, supramolecular interactions such as hydrogen bonds and  $\pi$ - $\pi$  bonds can be endowed to the pores, thereby enhancing the adsorption and activation of  $\text{CO}_2$ . To date, the combination of MOFs with semiconductors are mostly realized by direct mixing and physical adsorption, which leads to low charge carriers transfer efficiency between semiconductors and catalysts. Therefore, like the molecular catalyst/semiconductor catalytic system, the efficient and swift electron transfer between MOFs and semiconductors is also a frontier for researchers.

## 2.5. Microorganism/Semiconductor Biomimetic Interfaces

Since biological systems provide a relatively complete environment for utilizing solar energy in a more complex and effective way, microbial catalytic reduction of  $\text{CO}_2$  has unique advantages. Biological enzymes such as carbon monoxide dehydrogenase (CODHs), formate dehydrogenase (FDH), alcohol dehydrogenase (ADH), and formaldehyde dehydrogenase (FADH) can selectively convert  $\text{CO}_2$  to specific products at room temperature and atmospheric pressure. However, these reaction processes usually require expensive NADH as an auxiliary material.<sup>[81]</sup> In addition, the shortcomings of the biophotosynthetic system are also obvious, since the primary goal of biophotosynthesis for plants is survival instead of maximizing the conversion of solar energy. The photosynthesis efficiency of most plants is only 0.1%, while the highest efficiency is no more than 6%.<sup>[82]</sup>

Microbial electrosynthesis (MES) is a new bioelectrochemical technique developed over the past decade. Microbial electrosynthesis of  $\text{CO}_2$  refers to a process driven by external electrical energy in which electrochemically active carbon-fixing microorganisms take in  $\text{CO}_2$  as their only carbon source to convert it into value-added chemicals and fuels. Currently, the most common microorganisms used for  $\text{CO}_2$  reduction via MES include methanogens and acetogens.<sup>[83]</sup> These microorganisms can all convert  $\text{CO}_2$  with specificity at a relatively low cathode potential that is usually lower than -1.0 V versus SHE. Therefore, the combination of semiconductor nanocatalysts that possess excellent spectral absorption and photoelectric conversion capabilities with microorganisms can enhance the advantages of both to carry out the biomimetic PEC conversion of  $\text{CO}_2$ .

There are currently two microbial/semiconductor catalysis systems for  $\text{CO}_2$  reduction that have different sources of electrons. In one system, microorganisms directly obtain electrons from the surface of semiconductors and then react with protons and  $\text{CO}_2$  inside the microorganisms. A hybrid semiconductor

nanowire-bacteria system with anaerobic bacterium and *Sporomusa ovata* fixed on Si nanowire arrays was constructed (Figure 5a). This system utilized Si nanowires to capture light, providing energy for microorganisms and reducing  $\text{CO}_2$  to acetic acid at a relatively low overpotential (less than 200 mV) with a Faradaic efficiency as high as 90%; good stability was maintained even after 200 h of operation.<sup>[84]</sup> This method can also be used to endow nonphotosynthetic microorganisms with photosynthetic abilities. After the combination of *Moorella thermoacetica* and the photocatalyst CdS, the photoelectrons generated on CdS can be used to convert  $\text{CO}_2$  to acetic acid with a high quantum efficiency of up to  $85\% \pm 12\%$  (Figure 5b,c).<sup>[85]</sup> In the other system, microorganisms take the  $\text{H}_2$  generated from photocatalysis on the semiconductor and use it as an electron carrier to reduce  $\text{CO}_2$  inside the microorganisms. A hydrogen evolution electrocatalyst was used as the cathode to split water to produce hydrogen, and the highly biocompatible *Methanosarcina barkeri* was chosen as a biocatalyst for  $\text{CO}_2$  fixation so that  $\text{H}_2$  and  $\text{CO}_2$  could react in the microorganisms to produce  $\text{CH}_4$  (Figure 5d). The system achieved a total Faradaic efficiency of 86% over 7 d. After the anode and cathode were replaced with an InP photocathode and a  $\text{TiO}_2$  photoanode that possessed photocatalytic activity, the reaction could be driven under light without external input of electrical energy, and a FE of  $82 \pm 10\%$  was achieved on the  $n^+/\text{p-Si}/\text{NiMO}$  photocathode with a low overpotential of 175 mV.<sup>[86]</sup> Similarly, in the  $\text{CoP}_2|\text{Co-P}|$  *Ralstonia eutropha* hybrid system, *R. eutropha* bacteria can also utilize  $\text{H}_2$  generated by water splitting to convert  $\text{CO}_2$  into alcoholic liquid fuels and biomass. The energy efficiency of  $\text{CO}_2$  reduction has reached 10%, which is higher than that of the natural photosynthesis system.<sup>[87]</sup> The main difference between these two types of transformation systems is the method of electron transfer. Microbial systems that directly accept electrons from electrodes cannot be applied with excessively high current density during operation, since high current density can lead to the rapid generation of hydrogen and the shedding of microbial membranes. These phenomena inhibit electron transfer and lead to a slower reaction rate. In contrast, indirect electron transfer is limited by the solubility of  $\text{H}_2$  in water, resulting in a low mass transfer efficiency.

Microbial/semiconductor biomimetic PEC can efficiently and selectively convert  $\text{CO}_2$  over a long operating lifetime. However, due to the complexity of microbial systems, it is necessary to consider the biocompatibility of the corresponding semiconductor materials and the interactions between the microorganisms and semiconductors. Moreover, it is also essential to understand the mechanisms of extracellular electron transfer; such an understanding can be achieved by integrating knowledge from multidisciplinary fields such as electrochemistry, materials science, engineering, microbiology, metabolic engineering, and synthetic biology. Therefore, the directed conversion of  $\text{CO}_2$  into fuels and value-added chemicals can be improved.

Among these five semiconductor-based biomimetic catalytic interfaces, metal cocatalysts have been widely studied. They can widen the photoresponse range of semiconductors effectively and promote the rapid separation of photogenerated carriers, but more importantly, their nanoparticle morphology and size can be controlled and their crystal facets can be adjusted, enabling the efficient activation of  $\text{CO}_2$ . The activation configuration of  $\text{CO}_2$  is limited by the metal species, resulting in different

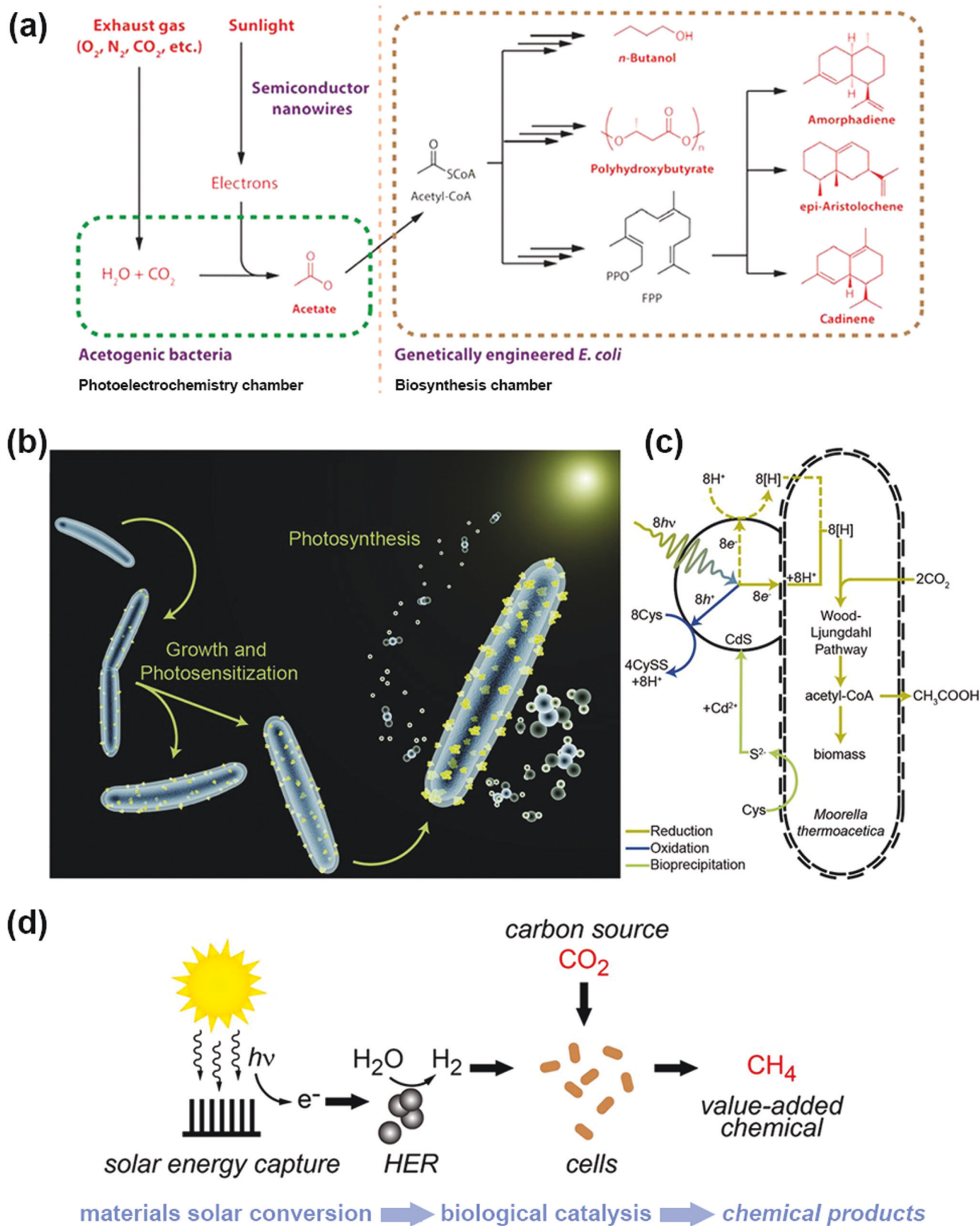


**Figure 5.** a) Schematic of a hybrid semiconductor nanowire-bacteria system which can convert exhaust gas into liquid fuels, biopolymers, and pharmaceutical precursors. Reproduced with permission.<sup>[84]</sup> Copyright 2015, American Chemical Society. b) Depiction of the *M. thermoacetica*-CdS hybrid

selectivities of CO<sub>2</sub> reduction products with different metal catalysts. However, compared with the other four types of biomimetic catalytic interfaces, the amount of CO<sub>2</sub> adsorption at the metal interface is insufficient. The advantage of small molecule catalysts is that they can be designed with –OH, –NH–, and other functional groups to introduce acid–base active sites, thereby enhancing the adsorption and activation of CO<sub>2</sub> at the interface. Molecular catalysts adsorb and activate CO<sub>2</sub> through the weak coordination bond between the central metal and CO<sub>2</sub> and its reduction intermediates. Such bonding clarifies the CO<sub>2</sub> reduction mechanism on molecular catalysts, but the products are often limited to C1 products such as CO and HCOOH. By changing the central metal atom and regulating and modifying the ligands, acid–base active sites and supramolecular forces such as hydrogen bonds and  $\pi$ – $\pi$  bonds are imparted to the porous 3D structure of MOF materials. Therefore, the adsorption and activation of CO<sub>2</sub> in the pores of MOFs are enhanced. The MOF/semiconductor biomimetic interface combines the advantages of the above three types of biomimetic catalytic interfaces. It is designable in terms of light absorption and CO<sub>2</sub> capture, adsorption, and activation. It is currently the most promising interface to fully simulate natural photosynthesis. The biomimetic microbial semiconductor interface uses microorganisms to metabolize CO<sub>2</sub> to convert CO<sub>2</sub>. Therefore, this type of biomimetic interface clearly enables the formation of CO<sub>2</sub> reduction products and it is expected to yield products with more carbon atoms. However, its shortcomings are also obvious; the CO<sub>2</sub> reduction products and reduction efficiency are determined by the metabolism of microorganisms, so the selection and cultivation of microorganisms and their harsh growth environments are limiting factors of the system.

Although biomimetic photoelectrocatalytic reduction of CO<sub>2</sub> is attracting extensive attention, the stability of photocathode has always been an important factor restricting the activity of catalytic CO<sub>2</sub>. Under illumination condition, electrons and holes can be formed on the semiconductor catalyst; however, these electrons and holes may induce photocorrosion due to the reduction or oxidation of the catalyst itself. Although the addition of voltage can alleviate photocorrosion, it is still a major problem that restricts the stability of catalysts. Researchers have made great efforts to find ways to enhance the stability of photocathodes. The ways to enhance the stability of the photocathode are summarized as follows. First, metal doping is an effective measure to mitigate photocorrosion. Metal doping on semiconductors enables the transfer of photogenerated electrons to metals and prevents the reduction of semiconductor catalysts. Liu et al. showed that photoelectrocatalytic CO<sub>2</sub> conversion to ethylene can be achieved by electrodeposition of Ag onto Cu<sub>2</sub>O with  $\approx 60\%$  Faradaic efficiency for hours, whereas bare Cu<sub>2</sub>O degrades within minutes.<sup>[88]</sup> Second, by constructing heterojunctions with other semiconductor materials, photocorrosion can be alleviated and the stability of

catalysts can be enhanced. The Cu<sub>2</sub>O has strong photocorrosivity, which significantly affects the stability of catalysts. Zhang et al. loaded SnO<sub>x</sub> onto Cu<sub>2</sub>O nanowires (NWs) as photocathode for PEC reduction of CO<sub>2</sub> to CO, which maintained long-term stability within 12 h.<sup>[89]</sup> Third, the unstable catalyst material can be encapsulated within the stable material to improve the stability of the catalyst. Wu et al. encapsulated Cu<sub>2</sub>O nanowires in MOFs of Cu<sub>3</sub>(BTC)<sub>2</sub> (BTC = 1,3,5-benzene tricarboxylate) for CO<sub>2</sub> reduction.<sup>[80]</sup> MOFs can not only suppress Cu<sub>2</sub>O corrosion induced by water vapor, but also promote charge separation and CO<sub>2</sub> adsorption, resulting in 1.9 times increase in the activity and stability of the nanocomposite for selective photocatalytic CO<sub>2</sub> reduction to methane. Fourth, the preparation method of the photoelectrode is also a factor affecting its stability. Currently, most of the catalyst materials are dispersed in Nafion and coated on the support electrodes (e.g., carbon paper, glassy carbon, fluorine-doped tin oxide), whereas this loading method may lead to poor catalyst stability due to uneven contact or weak binding between catalysts and substrates. The connection methods such as  $\pi$ – $\pi$  stacking<sup>[64]</sup> and in situ growth<sup>[90]</sup> can enhance the interaction between catalysts and substrates, thus improving photoelectrode stability and boosting charge transfer. More and more approaches are being explored to improve the stability of the photoelectrode for CO<sub>2</sub> reduction. Solving the problem of photoelectrode stability will lay the foundation for the rapid development of biomimetic photoelectrocatalysis of CO<sub>2</sub>.

### 3. Electron Transfer and Proton Coupling on the Biomimetic Photoelectrocatalytic Interface

In natural photosynthesis, water is oxidized by photogenerated holes to produce oxygen and provide protons for the fixation of CO<sub>2</sub> in the subsequent dark reaction.<sup>[8]</sup> CO<sub>2</sub> is then reduced via the Calvin cycle, which is a directed electron transfer process. Similar to natural photosynthesis, water can be oxidized at the anode of the biomimetic PEC interface, producing oxygen and protons.<sup>[23]</sup> Subsequently, CO<sub>2</sub> is reduced on the cathode via a directed electron transfer and proton coupling process to generate various products. This process is accompanied by an intricate mechanism involving multielectron transfer and proton coupling processes, resulting in poor product selectivity. Considering the complexity of the reaction on the biomimetic PEC interface, clarifying the electron transfer process between catalysts and semiconductors and elucidating the potential pathways of the CO<sub>2</sub>RR are of great importance. In this section, we illustrate the interfacial electron transfer process on different biomimetic PEC interfaces and summarize several possible reaction pathways for the reduction of CO<sub>2</sub> to different products. Moreover, proton coupling on the PEC interfaces is discussed according to different proton sources.

system, proceeding from the growth of the cells and bioprecipitation (loading) of the CdS nanoparticles (shown in yellow) through photosynthetic conversion of CO<sub>2</sub> (center right) to acetic acid (right), and c) pathway diagram for the *M. thermoacetica*–CdS system. Two possible routes to generate reducing equivalents, [H], exist: generation outside the cell (dashed line) or generation by direct electron transport to the cell (solid line). Reproduced with permission.<sup>[85]</sup> Copyright 2016, American Association for the Advancement of Science. d) General scheme depicting a hybrid bioinorganic approach to solar-to-chemical conversion. Sustainable energy inputs in the form of electrical potential or light can be used to generate hydrogen from water using inorganic HER catalysts; biological hydrogen-driven CO<sub>2</sub> fixation can subsequently generate value-added products such as methane. This materials biology interface can be generalized to other chemical intermediates and end products by mixing and matching different compatible inorganic and biological components. Adapted with permission.<sup>[86]</sup> Copyright 2015, National Academy of Sciences.

### 3.1. Electron Transfer and Product Regulation

As mimics of natural photosynthesis on the hybrid biomimetic PEC interface, modified materials, including metals, small molecules, molecular catalysts, MOFs and microorganisms, typically perform as active sites for CO<sub>2</sub> adsorption, activation and reduction, while semiconductors absorb light and supply active photogenerated electrons to facilitate the CO<sub>2</sub>RR. CO<sub>2</sub> is reduced by a directed electron transfer process on the biomimetic PEC interface. In contrast to PC and EC, the electrons on the PEC interface originate from two pathways: some electrons are photogenerated, while others are supplied by applied voltages. Under light irradiation at a specific wavelength, the semiconductor photocathode is excited and produces photogenerated electrons in the conduction band and holes in the valence band.<sup>[91]</sup> The applied electric field can facilitate the separation of charge carriers and drive the migration of photogenerated electrons to the surface of the cathode. Then, CO<sub>2</sub> is reduced to fuels on the cathode by the photogenerated electrons and the electrons provided by the applied voltage.

Interfacial electron transfer on different biomimetic PEC interfaces can be achieved by the potential difference between the catalyst and semiconductor, where the transfer driving force consists of the Schottky barrier, the difference between the conduction band minimum and the lowest unoccupied molecular orbital (LUMO) potential. At the metal cocatalyst/semiconductor biomimetic PEC interface, the Schottky junction between the metal particles and the semiconductor can promote the separation of charge carriers and cause the photogenerated electrons to accumulate on the metal cocatalysts. The electrons can then be transferred from the semiconductor to the cocatalyst under photoinduction, which is followed by the reduction of CO<sub>2</sub>.<sup>[92]</sup> At the small molecule/semiconductor biomimetic interface, small molecules act as electron donors and provide adsorption sites for the electrophilic C atoms of CO<sub>2</sub>, activating it. The supplementation of photogenerated electrons from the semiconductor can further improve this effect and reduce CO<sub>2</sub> (Figure 6a).<sup>[93]</sup> A molecular catalyst can be designed to precisely control the functionality, and it can act as the reduction center when a semiconductor is used as the light absorber, forming an efficient hybrid catalytic system. At the molecular catalyst/semiconductor biomimetic PEC interface, the semiconductor absorbs light to generate photoinduced electrons, which are transferred to the molecular catalyst along with the electrons emanating from the external circuit due to the match between the minimum position of the semiconductor conduction band and the potential of the lowest unoccupied molecular orbital (LUMO) of the molecular catalyst (Figure 6b,c).<sup>[94]</sup> MOFs are a unique category of molecular catalysts. The interfacial electron transfer at the MOF/semiconductor biomimetic PEC interface exhibits a trend similar to that of aforementioned molecular catalyst/semiconductor interface, implying that electron transfer from the semiconductor to the MOFs occurs (Figure 6d,e).<sup>[95]</sup> At the microorganism/semiconductor PEC interface, electron transfer proceeds from the (photo)electrode to the biocatalyst. The semiconductor and the external bias provide electrons for the biosynthesis process, while the microorganisms exhibit superior catalytic performance for CO<sub>2</sub> reduction (Figure 6f).<sup>[96]</sup>

After interfacial electron transfer from the semiconductor to the catalytic surface, the adsorbed CO<sub>2</sub> is reduced via a series of electron transfer processes. Since the carbon atom in CO<sub>2</sub> is in its highest valence state, a wide range of reduction products can form. The CO<sub>2</sub>RR may go through different reaction pathways to reach the same product by generating different intermediates. The reduction product depends on the number of transferred electrons, and the potential reaction pathway is related to the catalytic interface. After the formation of a bent CO<sub>2</sub>•<sup>-</sup> anion radical via a one-electron reduction of CO<sub>2</sub>, the intermediate \*COOH is generated via the protonation of the oxygen atom. Following one electron transfer process with subsequent desorption from the catalytic surface, CO is released.<sup>[97]</sup> Alternatively, CO<sub>2</sub>•<sup>-</sup> may also be reduced by the protonation of the carbon atom with oxygen atom adsorbed on catalytic surface to produce \*OCHO. This intermediate is then reduced to formate.<sup>[98]</sup>

Beyond the initial reduction products, the other C1/C2+ products can be derived from the further reduction of CO or HCOOH. HCOOH is generally accepted to be the key intermediate in the formation of formaldehyde.<sup>[99]</sup> After the reduction of CO<sub>2</sub> to formic acid, HCOOH is further reduced to formaldehyde via a sequential two-electron transfer process. The reported pathways of the formation of methanol and methane are dissimilar. Some investigations have reported HCOOH as the key intermediate in the formation of CH<sub>3</sub>OH.<sup>[100]</sup> For example, the DFT calculations (Figure 7a) on 2D MOF Cu<sub>3</sub>(HHTQ)<sub>2</sub> revealed that the hydrogenation of oxygen atoms to produce \*HCOOH releases less energy than the hydrogenation of carbon atoms to form \*OCH<sub>2</sub>O (0.88 vs 1.32 eV), indicating that the generation of the \*HCOOH intermediate is thermodynamically favorable.<sup>[100b]</sup> With one transferred electron and protonation at the oxygen atom, one molecule of H<sub>2</sub>O is released, and the \*CHO intermediate is formed. Adsorbed \*CH<sub>2</sub>O is considered another crucial CO<sub>2</sub> reduction intermediate, and it is subsequently reduced to \*CH<sub>2</sub>OH. Following further reduction with the transfer of one e<sup>-</sup>, \*CH<sub>3</sub>OH is generated and then desorbs from the catalytic interface. Alternatively, a reaction pathway of CO<sub>2</sub> reduction to CH<sub>3</sub>OH via the intermediate \*CO has been reported on the non-metal BP (111) catalytic surface.<sup>[101]</sup> In contrast to the aforementioned mechanism, \*OCH<sub>2</sub> is regarded as another key intermediate in addition to \*CO. DFT calculations (Figure 7b) indicated that the hydrogenation of \*CO to \*OCH is more favorable. With one transferred electron, \*OCH is reduced to \*OCH<sub>2</sub> by protonation at the carbon atom, which results in a lower free energy change. The intermediate \*OCH<sub>2</sub> is then reduced to \*OCH<sub>3</sub> via one H<sup>+</sup>/e<sup>-</sup> transfer to a carbon atom and is eventually reduced to \*CH<sub>3</sub>OH via another single-electron transfer step.

The formation of methane requires an eight-electron transfer reaction, which is initiated by the reduction of the intermediate \*CO to \*CHO. There are two potential pathways for the formation of CH<sub>4</sub> after the formation of \*CHO. One is the \*OCH<sub>2</sub> pathway, which involves the formation of \*OCH<sub>2</sub> and \*OCH<sub>3</sub>, in which the protonation of the carbon atom is favored and the O atom bonds with the catalytic surface. DFT calculations have shown that on a catalytic single-atom Zn surface, the O atom bonds with the single Zn atom, and the C atom is protonated after the formation of \*CHO, generating \*OCH<sub>2</sub> and \*OCH<sub>3</sub>.<sup>[102]</sup> Subsequently, \*OCH<sub>3</sub> is reduced to \*OCH<sub>4</sub>, thus releasing a CH<sub>4</sub> molecule and leaving \*OH bonded to the catalyst surface. The

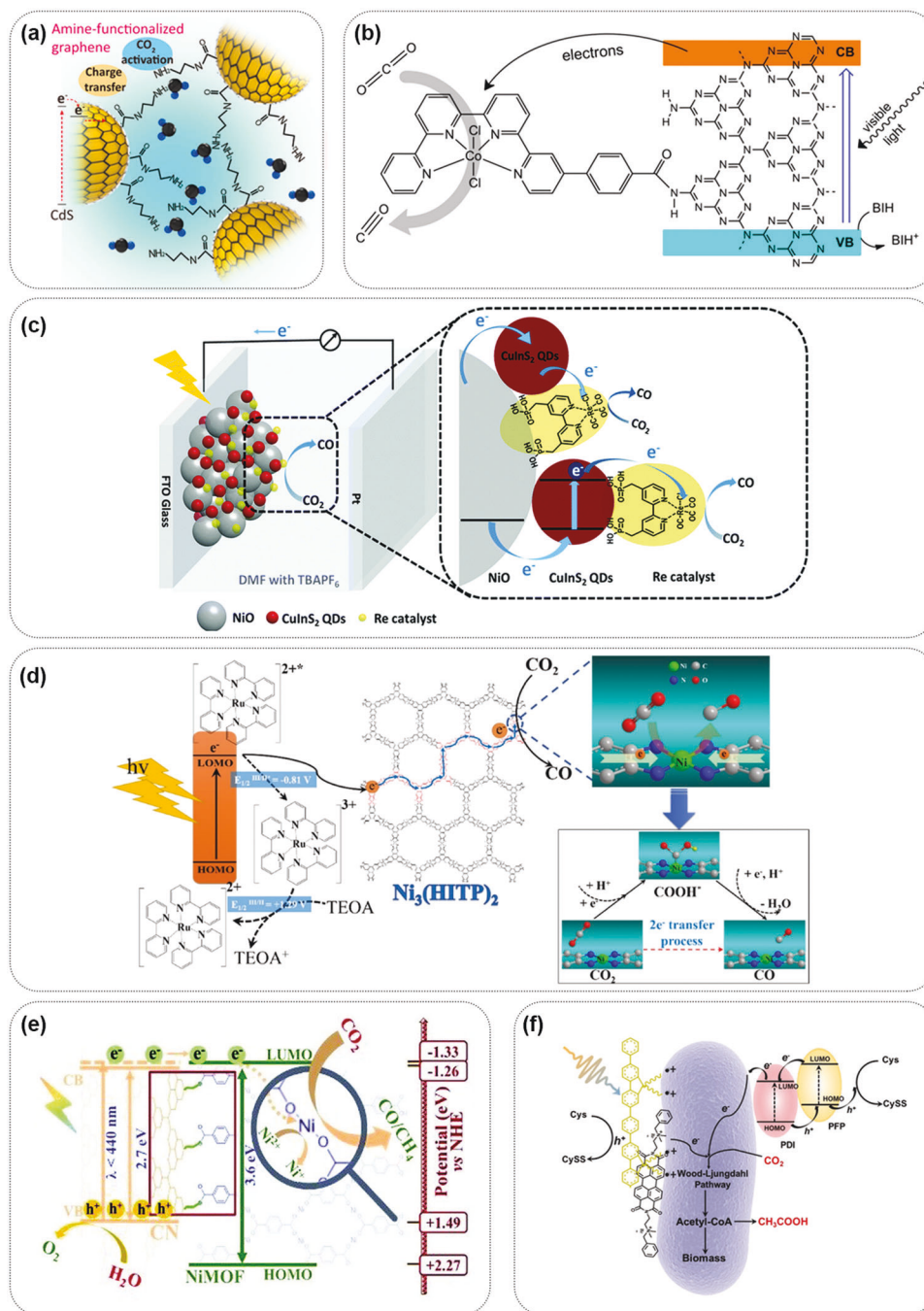


**Figure 6.** a) Graphical illustration of the proposed mechanism of  $\text{CO}_2$  photoreduction on the AG/CdS. Reproduced with permission.<sup>[93a]</sup> Copyright 2017, American Chemical Society. b) Illustration of the visible-light-driven  $\text{CO}_2$  to CO reduction process on Co-porphyrin@mesoporous graphitic  $\text{C}_3\text{N}_4$ . Reproduced with permission.<sup>[94b]</sup> Copyright 2020, American Chemical Society. c) Configuration of a PEC cell for  $\text{CO}_2$  reduction based on the NiO photocathode cografted with the  $\text{CuInS}_2$  QDs and the Re catalyst, and illustration of electron injection and hole transfer in the photocathode. Reproduced with permission.<sup>[94c]</sup> Copyright 2019, Royal Society of Chemistry. d) Proposed Mechanism of photocatalytic  $\text{CO}_2$  reduction to CO with  $\text{Ni}_3(\text{HITP})_2$  under visible-light irradiation. Reproduced with permission.<sup>[95a]</sup> Copyright 2018, Elsevier. e) A schematic diagram of the photogenerated charge transfer process and the induced photochemical reaction in the resultant NiMOF/functionalized CN nanocomposite. Reproduced with permission.<sup>[95b]</sup> Copyright 2020, Royal Society of Chemistry. f) Diagram of the photoexcited electron generated from PDI/PPF under illumination transferred by the membrane protein and finally passed on to the Wood-Ljungdahl pathway for  $\text{CO}_2$  reduction. Reproduced with permission.<sup>[96b]</sup> Copyright 2020, Wiley-VCH.

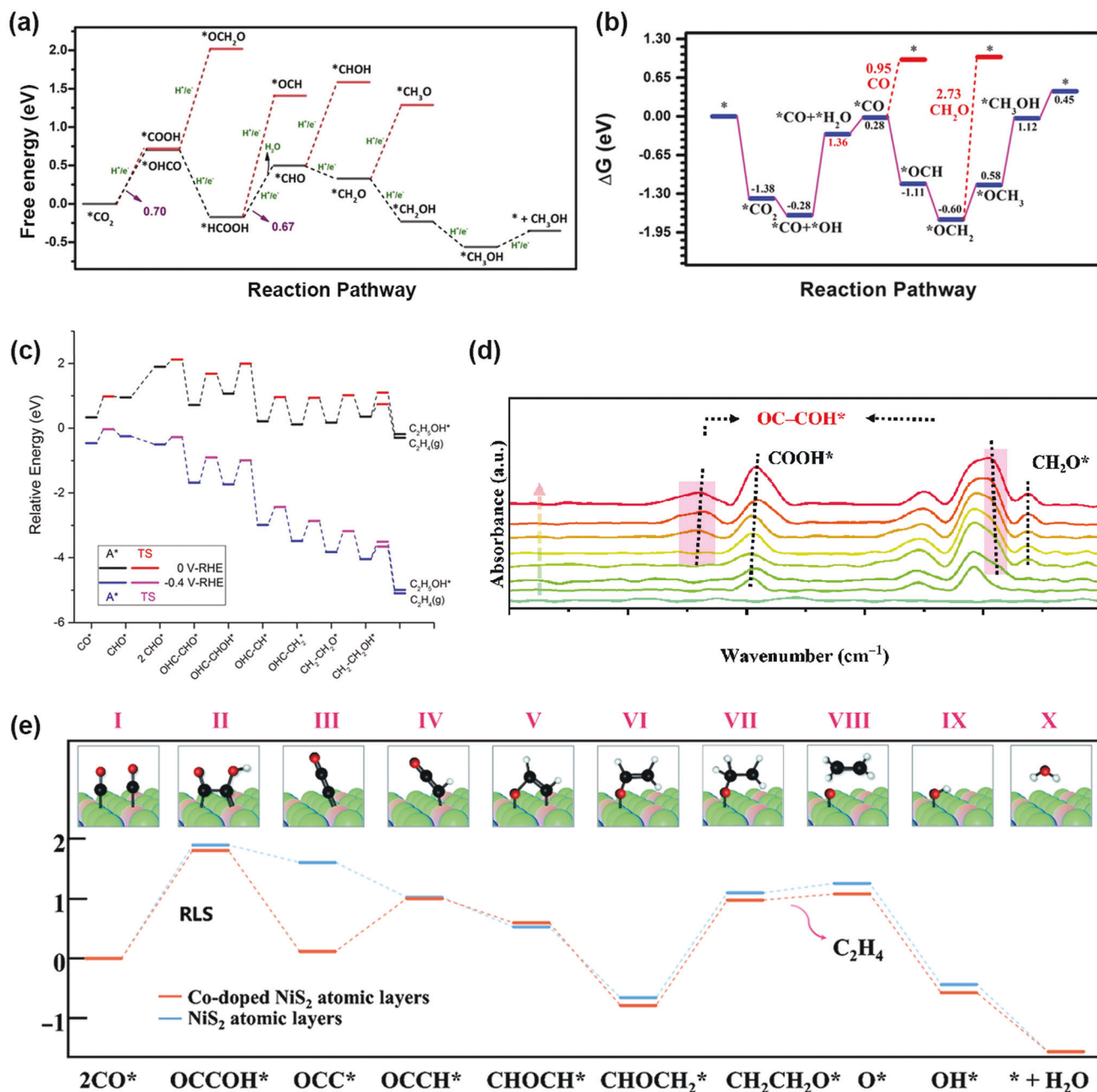


**Figure 7.** a) Free energy profiles for the CO<sub>2</sub>RR on Cu<sub>3</sub>(HHTQ)<sub>2</sub>. Reproduced with permission.<sup>[100b]</sup> Copyright 2021, Wiley-VCH. b) Free energy diagram of CO<sub>2</sub>RR on BP(111) surface. Reproduced with permission.<sup>[101]</sup> Copyright 2019, Wiley-VCH. c) Dominant path and associated reaction energetics identified for ethylene and ethanol production starting with CO\* on the Cu(100) facet at 0 V versus RHE and at -0.4 V versus RHE. Energy values are referenced to the CO<sub>2</sub>(g), H<sup>+</sup>(aq) + e<sup>-</sup> pair and a clean Cu(100) surface. Reproduced with permission.<sup>[104]</sup> Copyright 2016, American Chemical Society. d) In situ FTIR spectra measurements of reaction intermediates over the Co-doped NiS<sub>2</sub> atomic layers. e) Free energy diagrams of CO<sub>2</sub> reduction to C<sub>2</sub>H<sub>4</sub> for the Co-doped NiS<sub>2</sub> atomic layers and NiS<sub>2</sub> atomic layers. Reproduced with permission.<sup>[108]</sup> Copyright 2021, Springer Nature.

final step is the adsorption of one more proton to \*OH, producing H<sub>2</sub>O. The alternative pathway is the \*CHOH pathway. Following the formation of \*CHO, \*CHOH forms via the preferred protonation of the O atom. For instance, on the iridium-doped TiC catalyst, \*CHOH is found to be more stable than \*CH<sub>2</sub>O.<sup>[103]</sup> With an electron transfer, \*CHOH is reduced to \*CH with the generation of one molecule of H<sub>2</sub>O. Then, CH<sub>4</sub> forms through

three sequential single-electron transfers and the protonation of the carbon atom and then desorbs from the catalyst surface.

The formation of C<sub>2</sub>+ products is more complicated since it involves not only multielectron transfer but also C-C coupling. Although the pathways for the formation of C<sub>2</sub>+ products are elusive, it is generally accepted that CO<sub>2</sub> is first reduced to adsorbed \*CO, which is a key intermediate in the generation of C<sub>2</sub>+



products. Following the formation of  $^*CO$ , C–C coupling, one of the most crucial steps in  $CO_2$  reduction to  $C_2+$  compounds, occurs. Three potential mechanistic pathways of C–C coupling are proposed. In the first pathway, C–C coupling occurs after the formation of the  $^*CHO$  intermediate derived from the hydrogenation of carbon atoms by one-electron transfer.  $^*CHO$  preferentially forms on Cu(100), where C–C coupling to form  $C_2$  products is achieved by the dimerization of the  $^*CHO$  species.<sup>[104]</sup> The DFT calculations illustrated a barrier of 0.22 eV for the non-electrochemical coupling of  $^*CHO$  and  $^*CHO$ , which is lower than that of the coupling of  $^*CO$  and  $^*CHO$ , indicating that the C–C coupling kinetics can be promoted by increasing the hydrogenation degree of C1 intermediates. Compared with the competitive conversion of  $^*CHO$  to  $^*CH_2O$  which is the key intermediate for methanol and methane formation, adsorbed OHC–CHO is favored at low potentials since C–C coupling is a nonelectrochemical step. Following C–C coupling, a series of reduction reactions, including O–H bond formation, C–OH bond cleavage, and C–H bond formation, occur, producing  $C_2$  compounds (Figure 7c). The second pathway, the dimerization of  $^*CO$ , is considered a more prevalent C–C coupling mechanism and is reported in most studies. Given that CO is one of the main products of  $CO_2RR$ , surface coverage of  $^*CO$  is supposed to be larger than that of hydrogenated species.<sup>[105]</sup> Therefore, the C–C coupling via direct dimerization of  $^*CO$  is more likely to occur due to the high surface concentration of  $^*CO$ . This tendency can be verified by both electrochemical analysis and DFT calculations. For example, Meng et al.<sup>[106]</sup> reported a tandem catalyst PTF(Ni)/Cu constructed by dispersing Cu NPs on the porphyrinic triazine framework anchored with atomically isolated Ni- $N_4$  sites for highly selective electrocatalytic  $CO_2$  to  $C_2H_4$ . Operando ATR-FTIR studies confirmed the appearance of chemisorbed CO peak in the band located at  $2089\text{ cm}^{-1}$ . A large amount of  $^*CO$  is expected to trigger the formation of  $C_2+$  products. Furthermore, a band at  $1585\text{ cm}^{-1}$  was displayed, which can be assigned to the C–O stretching of  $^*COCO^-$  intermediate. The bands were red shift in the  $^{13}CO_2$  labeling ATR-FTIR experiments in KCl solution, indicating that the observed bands are ascribed to  $CO_2RR$  intermediates instead of carbonate or bicarbonate from electrolytes. DFT calculations further revealed the tandem mechanism that CO can be desorbed from PTF(Ni) and then migrate to the adjacent Cu(200) surface due to the lower adsorption energy at Cu(200). With the surface coverage of CO increasing, CO dimerization for the formation of  $^*OCCO$  with a significantly lower free energy (0.51 eV) is favored in comparison to the competitive hydrogenation of  $^*CO$  for the generation of  $^*CHO$ . After the rate-determining step,  $C_2H_4$  is produced via several intermediates such as  $^*OCCOH$ ,  $^*CCO$ , and  $^*CHCHO$  by a series of  $H^+/e^-$  transfer reaction on Cu(200) surface. In addition to tandem catalysis, nanoconfinement also provides an effective strategy for the promotion of C–C coupling by tuning the diffusion kinetics to achieve a high local concentration of C1 intermediates for their dimerization. For instance, a series of  $Cu_2O$  hollow multi-shell structures with different shell numbers were prepared based on the finite-element method simulation results, presenting a maximum  $C_2+$  FE of 77%. The nanoconfinement effect promotes the contact and interaction of reactants, meanwhile the restricted outflux of as-formed species can suppress the desorption of C1 intermediates. Current-step experiment and in situ electrochem-

ical Raman spectroscopy studies unraveled that the increase of shell number leads to a higher coverage of surface-absorbed CO for enhanced carbon dimerization.<sup>[107]</sup> Another evidence supporting the pathway of direct  $^*CO$  coupling is offered by mechanistic studies of  $CO_2$  photoreduction over Co-doped  $NiS_2$  atomic layers (Figure 7d,e). Via in situ FTIR measurements, absorption bands were observed at approximately  $1191$  and  $1672\text{ cm}^{-1}$  during photocatalytic  $CO_2$  reduction.<sup>[108]</sup> These two peaks can be ascribed to the C–OH and C=O stretching modes of the OC–COH intermediate, which is formed through the dimerization of  $^*CO$  and the protonation of the O atom. In the third pathway, C–C coupling may also occur between  $^*CO$  and  $^*CHO$ . Head-Gorden and co-workers proposed an alternative mechanism of C–C coupling between  $^*CO$  and  $^*CHO$  to derive  $C_2$  products over the (100) and (111) facets of Cu.<sup>[109]</sup> This mechanism identifies  $^*COCHO$  as the key intermediate in the reduction of  $CO_2$  to  $C_2$  products, as the DFT calculations indicate that at high potentials the reduction of CO to  $^*CHO$  with subsequent coupling with  $^*CO$  to form  $^*COCHO$  is more favorable than the dimerization of  $^*CO$ . In comparison to its tautomer  $^*COCO$ H, the structure of  $^*COCHO$  does not contain a double bond to the surface, thus presenting 0.43 eV more stable without an applied potential. These findings provide evidence for the proposed C–C bond formation mechanism.

### 3.2. Proton Coupling and Reaction Pathways

$CO_2$  is thermodynamically stable and kinetically inert, making its reduction difficult.<sup>[110]</sup> After the adsorption of  $CO_2$  molecules on the catalytic interface, the formation of  $CO_2\bullet^-$  anion radicals via a one-electron transfer process requires a high overpotential of  $-1.90\text{ V}$  to convert the linear molecular structure of  $CO_2$  to a bent anionic radical.<sup>[111]</sup> However, with proton coupling, the overpotential of the  $CO_2RR$  shifts to a more positive value, indicating a lower energy barrier.<sup>[112]</sup> This result suggests the significant role of protons in the reduction of  $CO_2$ . In natural photosynthesis, protons are produced by the light reaction where water is oxidized and then transferred by the proton transferase NADPH, which can supply recyclable protons for the  $CO_2RR$ . In the biomimetic PEC  $CO_2$  reduction, the source and supply route of protons can vary, and they include the dissociated protons provided by the electrolyte and the protons generated at the anode.

In aqueous electrolyte solution, water molecules are generally considered proton donors that participate in  $CO_2$  reduction. The mechanism by which water molecules near the cathode act as proton sources to promote the  $CO_2RR$  is proposed at the  $MoS_2$  interface.<sup>[113]</sup> DFT calculations imply that one proton dissociates from a water molecule near the cathode and then is transferred through the hydrogen bond chain; it then combines with  $^*CO_2$  to form a  $^*COOH$  intermediate with a relatively low free energy barrier of 0.21 eV. With the aid of the protons, the C–OH bond is broken to form  $^*CO$ , simultaneously producing a  $H_2O$  molecule.  $CO$  finally desorbs from the cathode surface, and the newly generated  $H_2O$  molecule participates in the reaction again and further lowers the energy barrier. In addition to water, some organic molecules serve as proton donors to facilitate the  $CO_2RR$ . For example, to suppress the competing HER, *n*-propanol (PrOH) has been employed as a weak proton donor in  $CO_2$  reduction by

FeTPP.<sup>[114]</sup> The presence of the weak proton donor favors the protonation of the C atom of CO<sub>2</sub>, leading to the selective production of formate. Inspired by natural photosynthesis, researchers have investigated NADH analogs as redox mediators for the enhanced catalytic performance of electrochemical CO<sub>2</sub> reduction by iron porphyrin (Figure 8a).<sup>[115]</sup> The redox reaction of NADH analogs can facilitate the two-electron/two-proton transfer process, supplying protons for the reduction of CO<sub>2</sub> to CO via a cyclic pathway. With the addition of a proton/electron donor, the catalytic activity for CO<sub>2</sub> reduction is enhanced 13-fold. Further experiments with different additives have shown that employing an electron-only additive enhances the rates of CO evolution over that of pristine Fe-TPP (8.4-fold), but these systems do not outperform NADH analogs that serve as both electron and proton sources, implying the significance of protons in improving the catalytic activity.

While they are often supplied by electrolytes or additives, protons can also be generated by water oxidation on the anode. For example, at a Nafion-coated TiO<sub>2</sub> interface, selective alcohol production was achieved due to the faster proton transport provided by the Nafion coating.<sup>[116]</sup> In the PEC CO<sub>2</sub> reduction system, protons are produced by the oxidization of water at the BiVO<sub>4</sub> photoanode. At the cathode, abundant protons are monitored by the functional Nafion coating, which promotes the fast transfer of protons and high proton concentrations around the cathode. After the formation of the CO<sub>2</sub>•<sup>-</sup> anion radical, a proton is transferred from the catholyte to CO<sub>2</sub>•<sup>-</sup>. Methanol and ethanol are generated through a series of proton-assisted electron transfer processes. Since electron transfer is kinetically favorable over proton transport, the proton concentration around the cathode determines the reaction rates. Thus, the abundant protons accelerate the protonation of CO<sub>2</sub>•<sup>-</sup> and the production of methanol by preventing the dimerization of CO<sub>2</sub>•<sup>-</sup>, whereas insufficient protons drive the dimerization of CO<sub>2</sub>•<sup>-</sup> to generate more ethanol. This result indicates that protons play an important role in tuning the product selectivity of the CO<sub>2</sub>RR. To supply sufficient protons for CO<sub>2</sub> reduction, water oxidation may be replaced by the oxidation of organics at the anode. For example, a paired PEC system reduces CO<sub>2</sub> to CH<sub>3</sub>OH at the cathode and while also promoting the oxidation of furfural to 2-furoic acid and 5-hydroxyfuroic acid at the anode (Figure 8b).<sup>[117]</sup> Under light irradiation, the photocathode is excited and produces photogenerated electrons and holes, while furfural, instead of water, is oxidized to generate more protons at the anode surface. These protons effectively participate in the PEC CO<sub>2</sub> reduction to CH<sub>3</sub>OH, increasing the product yield.

To directly supply protons from the catholyte to the catalytic surface without undergoing proton transfer, catalysts can be endowed with proton donor functions by design. For instance, efficient CO<sub>2</sub> reduction to CH<sub>4</sub> with the aid of protons provided by the oxidation of lattice hydroxyls on CoGeO<sub>2</sub>(OH)<sub>2</sub> photocatalyst surface has been reported (Figure 8c).<sup>[118]</sup> Under light irradiation, the surface lattice hydroxyl groups were oxidized by the photogenerated holes to produce protons and oxygen vacancies. The adsorption and activation of CO<sub>2</sub> were realized by capturing O atoms at the Lewis acid sites (the oxygen vacancies) and C atoms at the Lewis base sites (the hydroxyl groups). With the assistance of protons, the reaction kinetics of CO<sub>2</sub>RR were accelerated, promoting the formation of CH<sub>4</sub>. Instead of generating protons via the oxidization of surface hydroxyls, proton donor groups linked

to the catalyst can also serve as proton sources. For example, the proton donor H<sub>2</sub>Pc can facilitate the selective CO<sub>2</sub> reduction to CO on a conjugated composite microporous CoPc/H<sub>2</sub>Pc polymer catalyst (Figure 8d).<sup>[119]</sup> The measurement of kinetic isotope effect (KIE) indicated that the rate-determining step was the proton transfer process, and the addition of the proton donor, H<sub>2</sub>Pc, decreased the KIE value from 4.0 to 1.77, signifying accelerated proton transfer. The proton donor H<sub>2</sub>Pc lowered the energy barrier of the reduction of \*CO<sub>2</sub> to the \*COOH intermediate and the further reduction of \*COOH to \*CO. Finally, CO was desorbed from the Co reactive sites. In another example, Barton Cole et al.<sup>[120]</sup> investigated the homogeneous catalytic CO<sub>2</sub> reduction by pyridinium. They found that pyridinium can reduce CO<sub>2</sub> to CH<sub>3</sub>OH. Among these reaction pathways, the re-adsorption of intermediates (•COOH, •CHO, CH<sub>2</sub>O) on pyridinium and the reaction of pyridinium radicals to provide H• were predominant. Theoretical calculations revealed that the ΔG of the adsorption of the intermediates on pyridinium was greater than 0, and the reaction between the intermediates and the pyridinium radical to generate a product was spontaneous. If hydrogen atoms were continuously added after CO<sub>2</sub> adsorption, the ΔG of the adsorption process would remain less than 0.

Molecular catalysts can supply protons due to their specific molecular structures. The molecular catalyst system for CO<sub>2</sub> reduction is also the type of catalysis that is most similar to natural photosynthesis. The direct addition of H atoms to C promotes the generation of value-added C1 compounds. If the molecular catalyst can not only effectively adsorb CO<sub>2</sub> but also provide the H<sup>-</sup> that combines with C atoms, C1 compounds such as methane and methanol may be generated effectively. The biological coenzyme NADH, which is essential for the citric acid cycle, can provide one H<sup>+</sup> and two e<sup>-</sup> (equivalent to one H<sup>-</sup>). Tanaka's research team found that [Ru(pbn)(bpy)<sub>2</sub>](PF<sub>6</sub>)<sub>2</sub> (pbn = 2-(2-pyridyl)benzo[b]-1.5-naphthyridine, bpy = 2,2'-bipyridine) can be reduced to [Ru(pbnHH)(bpy)<sub>2</sub>](PF<sub>6</sub>)<sub>2</sub>; the structure of this complex is analogous to the coenzyme NADH under electrochemical conditions. It was also found that the Ru complex can transfer hydrides between molecules; it can directly transfer H<sup>-</sup> to the C atom in the carbonyl group of acetone. Subsequently, the research team studied the catalytic ability of [Ru(pbnHH)(bpy)<sub>2</sub>]<sup>2+</sup> in CO<sub>2</sub> reduction.<sup>[121]</sup> The C-H bonds can be formed through the transfer of H<sup>-</sup> with the aid of the benzoic acid anion, thereby reducing CO<sub>2</sub> to formic acid. Moreover, [Ru(pbn)(bpy)<sub>2</sub>]<sup>2+</sup> can be reduced again to [Ru(pbnHH)(bpy)<sub>2</sub>]<sup>2+</sup> by photocatalytic reduction; this is an example of molecular catalyst recycling. However, this type of molecular catalyst cannot provide abundant CO<sub>2</sub> adsorption sites and can only achieve the intermolecular transfer of H<sup>-</sup>. If intramolecular H<sup>-</sup> transfer can be achieved, the catalytic activity of the molecular catalyst may be further enhanced.

To compare the hydride transfer capacity of different molecular catalysts, Muckerman et al.<sup>[122]</sup> then calculated the hydricity of [Ru(pbnHH)(bpy)<sub>2</sub>]<sup>2+</sup> and other molecular catalysts. The calculated results showed that the hydride-donating ability of [Ru(pbnHH)(bpy)<sub>2</sub>]<sup>2+</sup> is not very strong, while the triply reduced and doubly protonated isomeric [Ru(pbnHH)(bpy)<sub>2</sub>•<sup>-</sup>]<sup>2+</sup> exhibited the most promising hydride-donating power. Moreover, it was found that the hydride transfer capacity of [Re(pbnHH)(CO)<sub>3</sub>Cl] is stronger than that of [Ru(pbnHH)(bpy)<sub>2</sub>]<sup>2+</sup>. According to the previous review on the

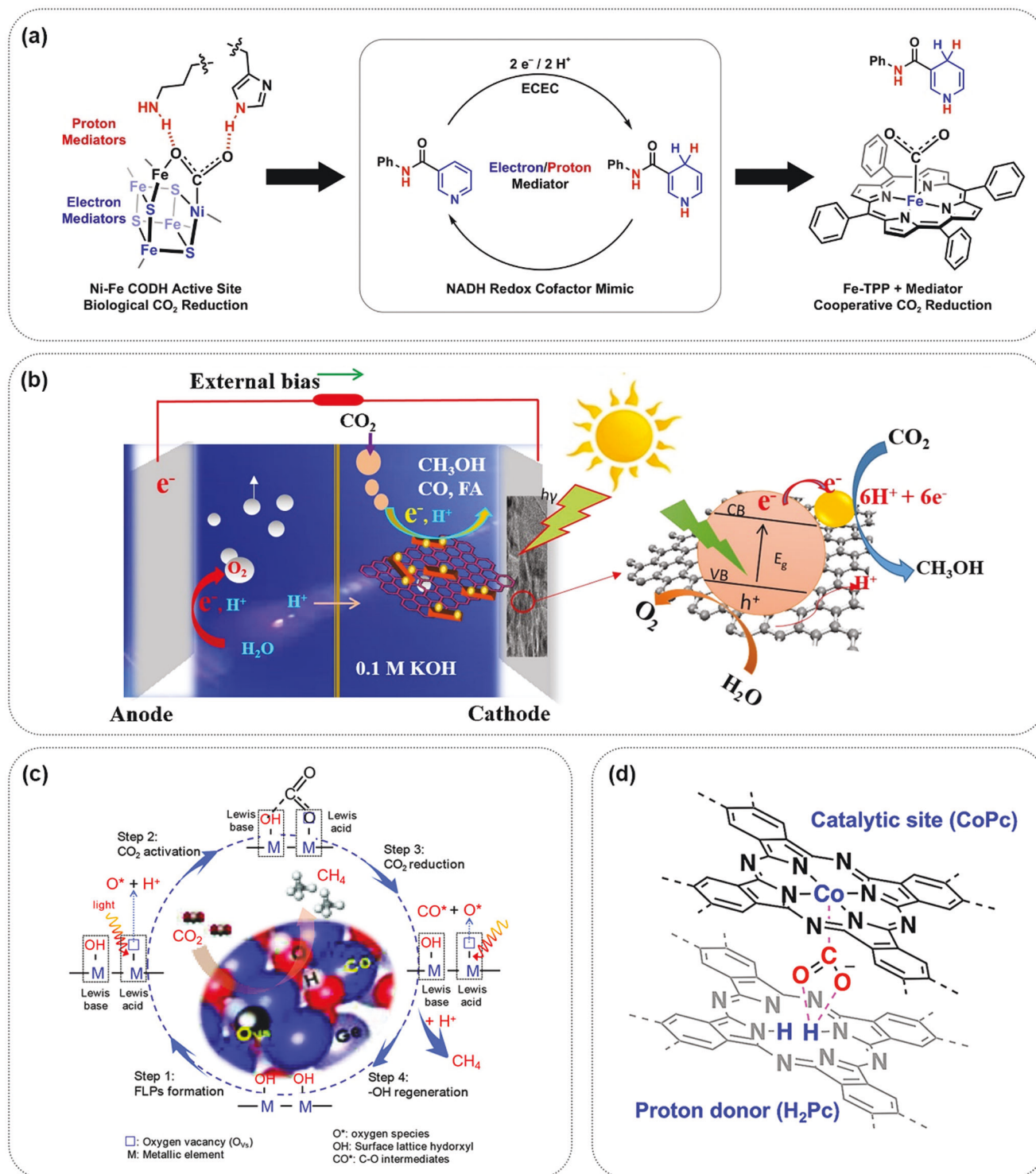


**Figure 8.** a) Bioinspired design of second-sphere additives that enable dual electron and proton control for facilitating electrochemical CO<sub>2</sub> reduction catalyzed by iron tetraphenylporphyrin (Fe-TPP). Reproduced with permission.<sup>[115]</sup> Copyright 2020, American Chemical Society. b) Proposed CO<sub>2</sub> reduction mechanism over the Au/α-Fe<sub>2</sub>O<sub>3</sub>/RGO photocathode. Reproduced with permission.<sup>[117]</sup> Copyright 2021, Elsevier. c) Possible four-step CH<sub>4</sub> generation mechanism for using the surface lattice hydroxyl as solid-state proton source. Reproduced with permission.<sup>[118]</sup> Copyright 2018, Wiley-VCH. d) Proposed proton-donor mechanism of H<sub>2</sub>Pc for the synergistic catalysis of CO<sub>2</sub> reduction. Reproduced with permission.<sup>[119]</sup> Copyright 2021, Wiley-VCH.

Re bipyridine complex, during the catalytic reduction process, this type of molecular catalysts can easily lose a  $\text{Cl}^-$  to form a five-coordinate compound, which provides an empty coordination site for the combination of  $\text{CO}_2$  with the complex.<sup>[123]</sup> In this way, the M–C bond can be formed and while intramolecular  $\text{H}^-$  transfer occurs simultaneously.

In summary, during  $\text{CO}_2$  reduction, as protons are coupled, the energy barrier of  $\text{CO}_2\text{RR}$  can be lowered and the catalytic reaction pathway can be altered, facilitating the conversion of  $\text{CO}_2$  with low energy consumption and high efficiency. The protons can not only be derived from the electrolyte and anodic oxidation reaction but also be provided directly by the catalyst. Additives may be added as extra proton donors, or the anodic water oxidation reaction can be replaced by the oxidation of organic compounds. However, the proton transfer efficiency is still limited by the diffusion rate more so than when protons are directly provided by catalyst. Therefore, to construct an excellent biomimetic PEC interface, it is necessary to consider the integration of enhanced  $\text{CO}_2$  adsorption, multisite activation, electron transfer, and proton coupling functions.

#### 4. Conclusions and Perspectives

Converting the greenhouse gas  $\text{CO}_2$  to value-added fuels and chemicals is a promising way to alleviate two global issues, energy shortages, and environmental deterioration. The efficient  $\text{CO}_2$  reduction reaction relies on the construction of catalytic interfaces and explorations of the underlying reaction mechanisms. Natural photosynthesis provides inspiration for the construction of catalytic interfaces to promote  $\text{CO}_2$  adsorption, activation, and  $\text{CO}_2$  conversion. Mimicking natural photosynthesis, biomimetic PEC exhibits the advantages of EC, which include oriented electron transfer, and the strengths of PC, which include reduced electrical energy consumption; therefore, this process has great potential for  $\text{CO}_2$  utilization. This review illustrates strategies for constructing biomimetic interfaces with enhanced  $\text{CO}_2$  adsorption, activation, and conversion. It describes catalyst modification, biomimetic catalytic interface design, electron transfer on the catalytic interface, and reaction mechanisms involving proton coupling and electron transfer to form different products. It provides a reference for the design and optimization of efficient biomimetic PEC systems. Among five biomimetic PEC interfaces, metal cocatalysts can broaden the photoresponse range of semiconductors and promote the rapid separation of photogenerated carriers. Furthermore, the controllable nanoparticle morphology and size and adjustable crystal facets enable the efficient activation of  $\text{CO}_2$ . Nevertheless, the adsorption of  $\text{CO}_2$  at the metal surface is insufficient compared to the other four types of PEC interfaces. The modification of small molecules can introduce acid-base active sites via functional groups such as  $-\text{OH}$  and  $-\text{NH}-$ , thereby enhancing the adsorption and activation of  $\text{CO}_2$ . By modifying the central metal atom and regulating the ligands, molecular catalysts exhibit high controllability of catalytic properties, but the products are often limited to C1 compounds such as CO and HCOOH. The MOF/semiconductor biomimetic PEC interface integrates the advantages of the above three types of hybrid catalytic interfaces. It is designable in terms of light absorption and  $\text{CO}_2$  adsorption and activation, presenting great potential in realizing a thorough simulation of natural photosyn-

thesis. The microorganism/semiconductor biomimetic interface enables the production of long-chain multicarbon compounds via the assistance of microbial metabolism. However, the product selectivity and reduction efficiency are limited by the selection of microorganisms and the harsh cultivation environments. Although many investigations on biomimetic PEC  $\text{CO}_2$  reduction and catalytic mechanisms have made great breakthroughs, challenges still remain and substantial efforts are required to further enhance the conversion rate and selectivity of  $\text{CO}_2\text{RR}$ .

First, the linkage between the decoration material and the semiconductor is usually a noncovalent interaction that is susceptible to leaching and losing its activity. Covalent attachment is a promising way to overcome this issue, which requires a stronger link between the catalysts and semiconductor substrates. Several strategies for fabricating hybrid PEC interfaces by covalent linkage assembly include chemical coordination, introducing anchoring groups (such as carboxylic acids, phosphonic acids, and hydroxamic acids) and electrochemical polymerization. Chemical bonding ensures efficient charge transfer between semiconductor electrodes and catalysts, thus facilitating the rapid conversion of  $\text{CO}_2$ .

Second, the reduction of  $\text{CO}_2$  to C1 compounds such as CO and formate can be achieved with a high selectivity on the reported PEC interfaces, though the selectivity of C2 products is still limited by the complex reaction pathways involving not only proton coupling and electron transfer processes but also C–C coupling. Although the formation of multicarbon compounds is challenging, natural photosynthesis can realize the oriented conversion of  $\text{CO}_2$  to glucose, which indicates plenty of scope for investigations on mimicking natural photosynthesis to obtain multicarbon products. In addition to mimicking photosynthesis to enhance  $\text{CO}_2$  fixation and activation on the PEC interface, emerging catalytic strategies such as tandem catalysis, confinement engineering, highly dispersed single- or dual-atom catalysts can be adopted to increase the local concentration of C1 intermediates, thus making the formation of C–C bond more likely to occur.

Third, since  $\text{CO}_2$  reduction on the biomimetic PEC interface is a complex process including both the multielectron transfer from the catalytic surface to the adsorbed  $\text{CO}_2$  molecules and the interfacial electron transfer between the catalyst and semiconductor, determining the underlying mechanism is challenging, especially for the formation of C2+ compounds; a lack of mechanistic understanding impedes the rational design of effective PEC interfaces. Although plenty of experimental efforts have been dedicated to identifying the potential reaction intermediates and pathways toward C2+ products, currently only a few species have been detected. Due to their high reactivity, the surface coverage of these intermediates can be extremely low at all applied potentials, making their detection challenging. Advanced characterization techniques, including operando surface-enhanced Raman scattering, attenuated total reflection (ATR)-IR, scanning electrochemical microscopy (SECM), and in situ X-ray absorption spectroscopy, should be employed to provide key evidence for the proposed reaction mechanisms. These experimental methods combined with theoretical calculations enable the determination of the reaction intermediates, reactive sites and the potential reaction pathways.

Although PC can reduce  $\text{CO}_2$  without additional energy input, directed electron transfer does not occur. There is still a long way

to go to fully utilize PC to simulate natural photosynthesis. EC can achieve directed electron transfer and supply electrons in a cycle, but much electrical energy is required owing to the high overpotential of CO<sub>2</sub>RR. Complementing the advantages of PC and EC, we consider that PEC CO<sub>2</sub> reduction is one of the most promising ways of thoroughly simulating natural photosynthesis in the short term. We believe that this review can provide researchers with inspiration for designing efficient biomimetic PEC interfaces to achieve a higher yield and better selectivity of CO<sub>2</sub> reduction products.

## Acknowledgements

S.X. and Q.S. contributed equally to this work. This work was financially supported by the National Natural Science Foundation of China (NSFC, No. 21876128, 22076140, 21537003, 22006100).

Open Access funding enabled and organized by Projekt DEAL.

## Conflict of Interest

The authors declare no conflict of interest.

## Keywords

CO<sub>2</sub> conversion, electron transfer, photoelectrocatalysis, reaction mechanisms

Received: July 8, 2022

Revised: August 4, 2022

Published online: August 25, 2022

- [1] A. Otto, T. Grube, S. Schiebahn, D. Stolten, *Energy Environ. Sci.* **2015**, *8*, 3283.
- [2] W. Lu, Y. Zhang, J. Zhang, P. Xu, *Ind. Eng. Chem. Res.* **2020**, *59*, 5536.
- [3] R. Shi, G. I. Waterhouse, T. Zhang, *Sol. RRL* **2017**, *1*, 1700126.
- [4] a) L. Zhang, Z.-J. Zhao, J. Gong, *Angew. Chem., Int. Ed.* **2017**, *56*, 11326; b) K. Li, B. Peng, T. Peng, *ACS Catal.* **2016**, *6*, 7485; c) H. Xie, T. Wang, J. Liang, Q. Li, S. Sun, *Nano Today* **2018**, *21*, 41.
- [5] P. Prabhu, V. Jose, J.-M. Lee, *Adv. Funct. Mater.* **2020**, *30*, 1910768.
- [6] A. Kumar, V. Hasija, A. Sudhaik, P. Raizada, Q. Van Le, P. Singh, T.-H. Pham, T. Kim, S. Ghotekar, V.-H. Nguyen, *Chem. Eng. J.* **2022**, *430*, 133031.
- [7] a) B. Zhu, K. Qiu, C. Shang, Z. Guo, *J. Mater. Chem. A* **2015**, *3*, 5212; b) K. Yang, C. Yu, Z. Yu, M. Zhu, W. Zhao, H. Chen, F. Pan, *Mater. Lett.* **2019**, *247*, 102.
- [8] a) X. Liu, S. Inagaki, J. Gong, *Angew. Chem., Int. Ed.* **2016**, *55*, 14924; b) Y. Wang, H. Suzuki, J. Xie, O. Tomita, D. J. Martin, M. Higashi, D. Kong, R. Abe, J. Tang, *Chem. Rev.* **2018**, *118*, 5201.
- [9] A. M. Appel, J. E. Bercaw, A. B. Bocarsly, H. Dobbek, D. L. DuBois, M. Dupuis, J. G. Ferry, E. Fujita, R. Hille, P. J. Kenis, C. A. Kerfeld, R. H. Morris, C. H. Peden, A. R. Portis, S. W. Ragsdale, T. B. Rauchfuss, J. N. Reek, L. C. Seefeldt, R. K. Thauer, G. L. Waldrop, *Chem. Rev.* **2013**, *113*, 6621.
- [10] a) Y. X. Pan, Y. You, S. Xin, Y. Li, G. Fu, Z. Cui, Y. L. Men, F. F. Cao, S. H. Yu, J. B. Goodenough, *J. Am. Chem. Soc.* **2017**, *139*, 4123; b) S. Wang, B. Y. Guan, X. W. Lou, *Energy Environ. Sci.* **2018**, *11*, 306.
- [11] a) R. R. Ikreedeegh, M. Tahir, *J. CO<sub>2</sub> Util.* **2021**, *43*, 101381; b) X.-K. Wang, J. Liu, L. Zhang, L.-Z. Dong, S.-L. Li, Y.-H. Kan, D.-S. Li, Y.-Q. Lan, *ACS Catal.* **2019**, *9*, 1726; c) X. Li, Y. Sun, J. Xu, Y. Shao, J. Wu, X. Xu, Y. Pan, H. Ju, J. Zhu, Y. Xie, *Nat. Energy* **2019**, *4*, 690; d) L. Wang, J. Wan, Y. Zhao, N. Yang, D. Wang, *J. Am. Chem. Soc.* **2019**, *141*, 2238.
- [12] X. Yang, D. Wang, *ACS Appl. Energy Mater.* **2018**, *1*, 6657.
- [13] K. Wang, Y. Ma, Y. Liu, W. Qiu, Q. Wang, X. Yang, M. Liu, X. Qiu, W. Li, J. Li, *Green Chem.* **2021**, *23*, 3207.
- [14] G. Hyun, J. T. Song, C. Ahn, Y. Ham, D. Cho, J. Oh, S. Jeon, *Proc. Natl. Acad. Sci. USA* **2020**, *117*, 5680.
- [15] G. Collins, E. Armstrong, D. McNulty, S. O'Hanlon, H. Geaney, C. O'Dwyer, *Sci. Technol. Adv. Mater.* **2016**, *17*, 563.
- [16] A. M. Appel, J. E. Bercaw, A. B. Bocarsly, H. Dobbek, D. L. DuBois, M. Dupuis, J. G. Ferry, E. Fujita, R. Hille, P. J. Kenis, *Chem. Rev.* **2013**, *113*, 6621.
- [17] a) X. Li, J. Yu, M. Jaroniec, X. Chen, *Chem. Rev.* **2019**, *119*, 3962; b) L. Sun, V. Reddu, A. C. Fisher, X. Wang, *Energy Environ. Sci.* **2020**, *13*, 374.
- [18] a) V. Kumaravel, J. Bartlett, S. C. Pillai, *ACS Energy Lett.* **2020**, *5*, 486; b) S. Zhang, Q. Fan, R. Xia, T. J. Meyer, *Acc. Chem. Res.* **2020**, *53*, 255; c) P. R. Yaashikaa, P. Senthil Kumar, S. J. Varjani, A. Saravanan, *J. CO<sub>2</sub> Util.* **2019**, *33*, 131.
- [19] a) G. Wang, J. Chen, Y. Ding, P. Cai, L. Yi, Y. Li, C. Tu, Y. Hou, Z. Wen, L. Dai, *Chem. Soc. Rev.* **2021**, *50*, 4993; b) J. Fu, K. Jiang, X. Qiu, J. Yu, M. Liu, *Mater. Today* **2020**, *32*, 222.
- [20] a) J. Ferreira de Brito, P. G. Corradini, A. B. Silva, L. H. Mascaro, *ChemElectroChem* **2021**, *8*, 4305; b) J. F. de Brito, G. G. Bessegato, J. A. L. Perini, L. D. de Moura Torquato, M. V. B. Zanoni, *J. CO<sub>2</sub> Util.* **2021**, *55*, 101810; c) N. Nandal, S. L. Jain, *Coord. Chem. Rev.* **2022**, *451*, 214271.
- [21] W. Zhang, Z. Jin, Z. Chen, *Adv. Sci.* **2022**, *9*, 2105204.
- [22] D. Ješić, D. L. Jurković, A. Pohar, L. Suhadolnik, B. Likozar, *Chem. Eng. J.* **2021**, *407*, 126799.
- [23] X. Chang, T. Wang, P. Yang, G. Zhang, J. Gong, *Adv. Mater.* **2019**, *31*, 1804710.
- [24] J. Ran, M. Jaroniec, S. Z. Qiao, *Adv. Mater.* **2018**, *30*, 1704649.
- [25] I. Shown, H.-C. Hsu, Y.-C. Chang, C.-H. Lin, P. K. Roy, A. Ganguly, C.-H. Wang, J.-K. Chang, C.-I. Wu, L.-C. Chen, *Nano Lett.* **2014**, *14*, 6097.
- [26] W. Hou, W. H. Hung, P. Pavaskar, A. Goepfert, M. Aykol, S. B. Cronin, *ACS Catal.* **2011**, *1*, 929.
- [27] Y. Wang, J. Yu, W. Xiao, Q. Li, *J. Mater. Chem. A* **2014**, *2*, 3847.
- [28] R. Lee, Y. Kumaresan, S. Y. Yoon, S. H. Um, I. K. Kwon, G. Y. Jung, *RSC Adv.* **2017**, *7*, 7469.
- [29] W.-N. Wang, W.-J. An, B. Ramalingam, S. Mukherjee, D. M. Niedzwiedzki, S. Gangopadhyay, P. Biswas, *J. Am. Chem. Soc.* **2012**, *134*, 11276.
- [30] S. Bai, X. Wang, C. Hu, M. Xie, J. Jiang, Y. Xiong, *Chem. Commun.* **2014**, *50*, 6094.
- [31] Q. Lu, F. Jiao, *Nano Energy* **2016**, *29*, 439.
- [32] a) K. P. Kuhl, E. R. Cave, D. N. Abram, T. F. Jaramillo, *Energy Environ. Sci.* **2012**, *5*, 7050; b) M. Gattrell, N. Gupta, A. Co, *J. Electroanal. Chem.* **2006**, *594*, 1. c) K. J. P. Schouten, Z. Qin, E. Pérez Gallent, M. T. Koper, *J. Am. Chem. Soc.* **2012**, *134*, 9864.
- [33] F. Studt, I. Sharafutdinov, F. Abild-Pedersen, C. F. Elkjær, J. S. Hummelshøj, S. Dahl, I. Chorkendorff, J. K. Nørskov, *Nat. Chem.* **2014**, *6*, 320.
- [34] P. Hirsunsit, *J. Phys. Chem. C* **2013**, *117*, 8262.
- [35] D. Kim, J. Resasco, Y. Yu, A. M. Asiri, P. Yang, *Nat. Commun.* **2014**, *5*, 4948.
- [36] S. Ma, M. Sadakiyo, M. Heima, R. Luo, R. T. Haasch, J. I. Gold, M. Yamauchi, P. J. Kenis, *J. Am. Chem. Soc.* **2017**, *139*, 47.
- [37] X. Sun, Q. Zhu, X. Kang, H. Liu, Q. Qian, Z. Zhang, B. Han, *Angew. Chem., Int. Ed.* **2016**, *55*, 6771.
- [38] S. t. Neațu, J. A. Maciá-Agulló, P. Concepción, H. Garcia, *J. Am. Chem. Soc.* **2014**, *136*, 15969.

- [39] Q. Shen, J. Ma, X. Huang, N. Yang, G. Zhao, *Appl. Catal., B* **2017**, 219, 45.
- [40] Q. Kang, T. Wang, P. Li, L. Liu, K. Chang, M. Li, J. Ye, *Angew. Chem., Int. Ed.* **2015**, 54, 841.
- [41] Q. Chen, X. Chen, M. Fang, J. Chen, Y. Li, Z. Xie, Q. Kuang, L. Zheng, *J. Mater. Chem. A* **2019**, 7, 1334.
- [42] Z. Sun, W. Fang, L. Zhao, H. Wang, *Appl. Surf. Sci.* **2020**, 504, 144347.
- [43] L. J. Murphy, K. N. Robertson, R. A. Kemp, H. M. Tuononen, J. A. Clyburne, *Chem. Commun.* **2015**, 51, 3942.
- [44] H. Yu, R. Shi, Y. Zhao, G. I. Waterhouse, L. Z. Wu, C. H. Tung, T. Zhang, *Adv. Mater.* **2016**, 28, 9454.
- [45] S. Guo, S. Zhao, J. Gao, C. Zhu, X. Wu, Y. Fu, H. Huang, Y. Liu, Z. Kang, *Nanoscale* **2017**, 9, 298.
- [46] M. S. Xie, B. Y. Xia, Y. Li, Y. Yan, Y. Yang, Q. Sun, S. H. Chan, A. Fisher, X. Wang, *Energy Environ. Sci.* **2016**, 9, 1687.
- [47] P. Xia, B. Zhu, J. Yu, S. Cao, M. Jaroniec, *J. Mater. Chem. A* **2017**, 5, 3230.
- [48] Q. Zhu, Y. Cao, Y. Tao, T. Li, Y. Zhang, H. Shang, J. Song, G. Li, *J. CO<sub>2</sub> Util.* **2021**, 54, 101781.
- [49] C. Kim, T. Eom, M. S. Jee, H. Jung, H. Kim, B. K. Min, Y. J. Hwang, *ACS Catal.* **2017**, 7, 779.
- [50] Z. Sun, J. M. T. A. Fischer, Q. Li, J. Hu, Q. Tang, H. Wang, Z. Wu, M. Hankel, D. J. Searles, L. Wang, *Appl. Catal., B* **2017**, 216, 146.
- [51] D. Yang, H. Yu, T. He, S. Zuo, X. Liu, H. Yang, B. Ni, H. Li, L. Gu, D. Wang, *Nat. Commun.* **2019**, 10, 3844.
- [52] a) B. J. Fisher, R. Eisenberg, *J. Am. Chem. Soc.* **1980**, 102, 7361; b) M. Beley, J.-P. Collin, R. Ruppert, J.-P. Sauvage, *J. Chem. Soc., Chem. Commun.* **1984**, 1315; c) R. Angamuthu, P. Byers, M. Lutz, A. L. Spek, E. Bouwman, *Science* **2010**, 327, 313.
- [53] a) J. Hawecker, J.-M. Lehn, R. Ziessel, *J. Chem. Soc., Chem. Commun.* **1983**, 536; b) *J. Chem. Soc., Chem. Commun.* **1985**, 56; c) C. Bruckmeier, M. W. Lehenmeier, R. Reithmeier, B. Rieger, J. Herranz, C. Kavakli, *Dalton Trans.* **2012**, 41, 5026; d) C. W. Machan, S. A. Chabolla, J. Yin, M. K. Gilson, F. A. Tezcan, C. P. Kubiak, *J. Am. Chem. Soc.* **2014**, 136, 14598; e) C. Riplinger, M. D. Sampson, A. M. Ritzmann, C. P. Kubiak, E. A. Carter, *J. Am. Chem. Soc.* **2014**, 136, 16285.
- [54] a) D. L. DuBois, A. Miedaner, R. C. Haltiwanger, *J. Am. Chem. Soc.* **1991**, 113, 8753; b) J. W. Raebiger, J. W. Turner, B. C. Noll, C. J. Curtis, A. Miedaner, B. Cox, D. L. DuBois, *Organometallics* **2006**, 25, 3345.
- [55] a) J.-H. Jeoung, H. Dobbek, *Science* **2007**, 318, 1461; b) H. Dobbek, L. Gremer, R. Kiefersauer, R. Huber, O. Meyer, *Proc. Natl. Acad. Sci. USA* **2002**, 99, 15971; c) B. D. Yuhas, C. Prasittichai, J. T. Hupp, M. G. Kanatzidis, *J. Am. Chem. Soc.* **2011**, 133, 15854.
- [56] S. Sato, T. Morikawa, S. Saeki, T. Kajino, T. Motohiro, *Angew. Chem., Int. Ed.* **2010**, 49, 5101.
- [57] X. Huang, Q. Shen, J. Liu, N. Yang, G. Zhao, *Energy Environ. Sci.* **2016**, 9, 3161.
- [58] T. M. Suzuki, H. Tanaka, T. Morikawa, M. Iwaki, S. Sato, S. Saeki, M. Inoue, T. Kajino, T. Motohiro, *Chem. Commun.* **2011**, 47, 8673.
- [59] S. A. Yao, R. E. Ruther, L. Zhang, R. A. Franking, R. J. Hamers, J. F. Berry, *J. Am. Chem. Soc.* **2012**, 134, 15632.
- [60] C. L. Anfuso, R. C. Snoberger III, A. M. Ricks, W. Liu, D. Xiao, V. S. Batista, T. Lian, *J. Am. Chem. Soc.* **2011**, 133, 6922.
- [61] K. Sekizawa, K. Maeda, K. Domen, K. Koike, O. Ishitani, *J. Am. Chem. Soc.* **2013**, 135, 4596.
- [62] S. Oh, J. R. Gallagher, J. T. Miller, Y. Surendranath, *J. Am. Chem. Soc.* **2016**, 138, 1820.
- [63] M. Schreier, J. Luo, P. Gao, T. Moehl, M. T. Mayer, M. Grätzel, *J. Am. Chem. Soc.* **2016**, 138, 1938.
- [64] J. Liu, H. Shi, Q. Shen, C. Guo, G. Zhao, *Green Chem.* **2017**, 19, 5900.
- [65] a) A. Kumar, D. G. Madden, M. Lusi, K. J. Chen, E. A. Daniels, T. Curtin, J. J. Perry IV, M. J. Zaworotko, *Angew. Chem., Int. Ed.* **2015**, 54, 14372; b) C. V. McGuire, R. S. Forgan, *Chem. Commun.* **2015**, 51, 5199; c) Z. Zhang, Z.-Z. Yao, S. Xiang, B. Chen, *Energy Environ. Sci.* **2014**, 7, 2868; d) S. Wang, X. Wang, *Small* **2015**, 11, 3097.
- [66] M. Fernandez, P. G. Boyd, T. D. Daff, M. Z. Aghaji, T. K. Woo, *J. Phys. Chem. Lett.* **2014**, 5, 3056.
- [67] J. Albo, D. Vallejo, G. Beobide, O. Castillo, P. Castaño, A. Irabien, *ChemSusChem* **2017**, 10, 1100.
- [68] R. Shimoni, Z. Shi, S. Binyamin, Y. Yang, I. Liberman, R. Ifraemov, S. Mukhopadhyay, L. Zhang, I. Hod, *Angew. Chem., Int. Ed.* **2022**, 61, e202206085.
- [69] J.-D. Yi, D.-H. Si, R. Xie, Q. Yin, M.-D. Zhang, Q. Wu, G.-L. Chai, Y.-B. Huang, R. Cao, *Angew. Chem., Int. Ed.* **2021**, 60, 17108.
- [70] Y. Fu, D. Sun, Y. Chen, R. Huang, Z. Ding, X. Fu, Z. Li, *Angew. Chem., Int. Ed.* **2012**, 51, 3364.
- [71] Q. Liu, Z.-X. Low, L. Li, A. Razmjou, K. Wang, J. Yao, H. Wang, *J. Mater. Chem. A* **2013**, 1, 11563.
- [72] R. Li, J. Hu, M. Deng, H. Wang, X. Wang, Y. Hu, H. L. Jiang, J. Jiang, Q. Zhang, Y. Xie, *Adv. Mater.* **2014**, 26, 4783.
- [73] S. Wang, J. Lin, X. Wang, *Phys. Chem. Chem. Phys.* **2014**, 16, 14656.
- [74] S. Wang, X. Wang, *Appl. Catal., B* **2015**, 162, 494.
- [75] D. Tan, J. Zhang, L. Yao, X. Tan, X. Cheng, Q. Wan, B. Han, L. Zheng, J. Zhang, *Nano Res.* **2020**, 13, 768.
- [76] a) H. Jung, S. Y. Lee, C. W. Lee, M. K. Cho, D. H. Won, C. Kim, H.-S. Oh, B. K. Min, Y. J. Hwang, *J. Am. Chem. Soc.* **2019**, 141, 4624; b) Y. Gao, Q. Wu, X. Liang, Z. Wang, Z. Zheng, P. Wang, Y. Liu, Y. Dai, M.-H. Whangbo, B. Huang, *Adv. Sci.* **2020**, 7, 1902820.
- [77] F. Bayat, S. Sheibani, *Mater. Res. Bull.* **2022**, 145, 111561.
- [78] R. Gusain, P. Kumar, O. P. Sharma, S. L. Jain, O. P. Khatri, *Appl. Catal., B* **2016**, 181, 352.
- [79] Y. A. Wu, I. McNulty, C. Liu, K. C. Lau, Q. Liu, A. P. Paulikas, C.-J. Sun, Z. Cai, J. R. Guest, Y. Ren, V. Stamenkovic, L. A. Curtiss, Y. Liu, T. Rajh, *Nat. Energy* **2019**, 4, 957.
- [80] H. Wu, X. Y. Kong, X. Wen, S. P. Chai, E. C. Lovell, J. Tang, Y. H. Ng, *Angew. Chem., Int. Ed.* **2021**, 60, 8455.
- [81] R. K. Yadav, G. H. Oh, N.-J. Park, A. Kumar, K.-j. Kong, J.-O. Baeg, *J. Am. Chem. Soc.* **2014**, 136, 16728.
- [82] N. Kornienko, J. Z. Zhang, K. K. Sakimoto, P. Yang, E. Reisner, *Nat. Nanotechnol.* **2018**, 13, 890.
- [83] a) H.-Y. Yang, B.-L. Bao, J. Liu, Y. Qin, Y.-R. Wang, K.-Z. Su, J.-C. Han, Y. Mu, *Bioelectrochemistry* **2018**, 119, 180; b) A. a. Ragab, K. P. Katuri, M. Ali, P. E. Saikaly, *Front. Microbiol.* **2019**, 10, 1747; c) F. Ammam, P.-L. Tremblay, D. M. Lizak, T. Zhang, *Biotechnol. Biofuels* **2016**, 9, 163.
- [84] C. Liu, J. J. Gallagher, K. K. Sakimoto, E. M. Nichols, C. J. Chang, M. C. Chang, P. Yang, *Nano Lett.* **2015**, 15, 3634.
- [85] K. K. Sakimoto, A. B. Wong, P. Yang, *Science* **2016**, 351, 74.
- [86] E. M. Nichols, J. J. Gallagher, C. Liu, Y. Su, J. Resasco, Y. Yu, Y. Sun, P. Yang, M. C. Chang, C. J. Chang, *Proc. Natl. Acad. Sci. USA* **2015**, 112, 11461.
- [87] C. Liu, B. C. Colón, M. Ziesack, P. A. Silver, D. G. Nocera, *Science* **2016**, 352, 1210.
- [88] G. Liu, F. Zheng, J. Li, G. Zeng, Y. Ye, D. M. Larson, J. Yano, E. J. Crumlin, J. W. Ager, L.-w. Wang, F. M. Toma, *Nat. Energy* **2021**, 6, 1124.
- [89] Y. Zhang, D. Pan, Y. Tao, H. Shang, D. Zhang, G. Li, H. Li, *Adv. Funct. Mater.* **2022**, 32, 2109600.
- [90] Q. Shen, X. Huang, J. Liu, C. Guo, G. Zhao, *Appl. Catal., B* **2017**, 201, 70.
- [91] C. Jiang, S. J. A. Moniz, A. Wang, T. Zhang, J. Tang, *Chem. Soc. Rev.* **2017**, 46, 4645.
- [92] a) Y. Zhu, Z. Xu, Q. Lang, W. Jiang, Q. Yin, S. Zhong, S. Bai, *Appl. Catal., B* **2017**, 206, 282; b) Y. J. Jang, J.-W. Jang, J. Lee, J. H. Kim, H. Kumagai, J. Lee, T. Minegishi, J. Kubota, K. Domen, J. S. Lee, *Energy Environ. Sci.* **2015**, 8, 3597; c) Q. Chen, W. Mo, G. Yang, S. Zhong, H. Lin, J. Chen, S. Bai, *Small* **2021**, 17, 2102105.

- [93] a) K. M. Cho, K. H. Kim, K. Park, C. Kim, S. Kim, A. Al-Saggaf, I. Gereige, H.-T. Jung, *ACS Catal.* **2017**, *7*, 7064; b) Q. Huang, J. Yu, S. Cao, C. Cui, B. Cheng, *Appl. Surf. Sci.* **2015**, *358*, 350.
- [94] a) K. Maeda, *Adv. Mater.* **2019**, *31*, 1808205; b) B. Ma, G. Chen, C. Fave, L. Chen, R. Kuriki, K. Maeda, O. Ishitani, T.-C. Lau, J. Bonin, M. Robert, *J. Am. Chem. Soc.* **2020**, *142*, 6188; c) J. Huang, B. Xu, L. Tian, P. B. Pati, A. S. Etman, J. Sun, L. Hammarström, H. Tian, *Chem. Commun.* **2019**, *55*, 7918; d) B. Shan, S. Vanka, T.-T. Li, L. Troian-Gautier, M. K. Brennaman, Z. Mi, T. J. Meyer, *Nat. Energy* **2019**, *4*, 290.
- [95] a) W. Zhu, C. Zhang, Q. Li, L. Xiong, R. Chen, X. Wan, Z. Wang, W. Chen, Z. Deng, Y. Peng, *Appl. Catal., B* **2018**, *238*, 339; b) L. Zhao, Z. Zhao, Y. Li, X. Chu, Z. Li, Y. Qu, L. Bai, L. Jing, *Nanoscale* **2020**, *12*, 10010; c) L. Wang, P. Jin, S. Duan, H. She, J. Huang, Q. Wang, *Sci. Bull.* **2019**, *64*, 926; d) F. Yu, X. Jing, Y. Wang, M. Sun, C. Duan, *Angew. Chem., Int. Ed.* **2021**, *60*, 24849.
- [96] a) H. Zhang, H. Liu, Z. Tian, D. Lu, Y. Yu, S. Cestellos-Blanco, K. K. Sakimoto, P. Yang, *Nat. Nanotechnol.* **2018**, *13*, 900; b) P. Gai, W. Yu, H. Zhao, R. Qi, F. Li, L. Liu, F. Lv, S. Wang, *Angew. Chem., Int. Ed.* **2020**, *59*, 7224.
- [97] J. Shen, R. Kortlever, R. Kas, Y. Y. Birdja, O. Diaz-Morales, Y. Kwon, I. Ledezma-Yanez, K. J. P. Schouten, G. Mul, M. T. Koper, *Nat. Commun.* **2015**, *6*, 8177.
- [98] Q. Gong, P. Ding, M. Xu, X. Zhu, M. Wang, J. Deng, Q. Ma, N. Han, Y. Zhu, J. Lu, *Nat. Commun.* **2019**, *10*, 2807.
- [99] a) K. Nakata, T. Ozaki, C. Terashima, A. Fujishima, Y. Einaga, *Angew. Chem., Int. Ed.* **2014**, *53*, 871; b) S. Barman, S. Sreejith, S. Garai, R. Pochamoni, S. Roy, *ChemPhotoChem* **2019**, *3*, 93; c) H. R. Park, A. U. Pawar, U. Pal, T. Zhang, Y. S. Kang, *Nano Energy* **2021**, *79*, 105483.
- [100] a) S. Xu, L. Li, E. A. Carter, *J. Am. Chem. Soc.* **2018**, *140*, 16749; b) J. Liu, D. Yang, Y. Zhou, G. Zhang, G. Xing, Y. Liu, Y. Ma, O. Terasaki, S. Yang, L. Chen, *Angew. Chem., Int. Ed.* **2021**, *60*, 14473; c) C.-H. Lim, A. M. Holder, J. T. Hynes, C. B. Musgrave, *J. Am. Chem. Soc.* **2014**, *136*, 16081.
- [101] S. Mou, T. Wu, J. Xie, Y. Zhang, L. Ji, H. Huang, T. Wang, Y. Luo, X. Xiong, B. Tang, *Adv. Mater.* **2019**, *31*, 1903499.
- [102] L. Han, S. Song, M. Liu, S. Yao, Z. Liang, H. Cheng, Z. Ren, W. Liu, R. Lin, G. Qi, *J. Am. Chem. Soc.* **2020**, *142*, 12563.
- [103] S. Back, Y. Jung, *ACS Energy Lett.* **2017**, *2*, 969.
- [104] W. Luo, X. Nie, M. J. Janik, A. Asthagiri, *ACS Catal.* **2016**, *6*, 219.
- [105] T. K. Todorova, M. W. Schreiber, M. Fontecave, *ACS Catal.* **2019**, *10*, 1754.
- [106] D.-L. Meng, M.-D. Zhang, D.-H. Si, M.-J. Mao, Y. Hou, Y.-B. Huang, R. Cao, *Angew. Chem., Int. Ed.* **2021**, *60*, 25485.
- [107] C. Liu, M. Zhang, J. Li, W. Xue, T. Zheng, C. Xia, J. Zeng, *Angew. Chem., Int. Ed.* **2022**, *61*, e202113498.
- [108] W. Shao, X. Li, J. Zhu, X. Zu, L. Liang, J. Hu, Y. Pan, J. Zhu, W. Yan, Y. Sun, *Nano Res.* **2022**, *15*, 1882.
- [109] A. J. Garza, A. T. Bell, M. Head-Gordon, *ACS Catal.* **2018**, *8*, 1490.
- [110] W. Gao, S. Liang, R. Wang, Q. Jiang, Y. Zhang, Q. Zheng, B. Xie, C. Y. Toe, X. Zhu, J. Wang, L. Huang, Y. Gao, Z. Wang, C. Jo, Q. Wang, L. Wang, Y. Liu, B. Louis, J. Scott, A.-C. Roger, R. Amal, H. He, S.-E. Park, *Chem. Soc. Rev.* **2020**, *49*, 8584.
- [111] J. Wu, Y. Huang, W. Ye, Y. Li, *Adv. Sci.* **2017**, *4*, 1700194.
- [112] X. Cao, D. Tan, B. Wulan, K. Hui, K. Hui, J. Zhang, *Small Methods* **2021**, *5*, 2100700.
- [113] M. Asadi, M. H. Motevaselian, A. Moradzadeh, L. Majidi, M. Esmaeilirad, T. V. Sun, C. Liu, R. Bose, P. Abbasi, P. Zapol, *Adv. Energy Mater.* **2019**, *9*, 1803536.
- [114] C. G. Margarit, N. G. Asimow, C. Costentin, D. G. Nocera, *ACS Energy Lett.* **2019**, *5*, 72.
- [115] P. T. Smith, S. Weng, C. J. Chang, *Inorg. Chem.* **2020**, *59*, 9270.
- [116] M. J. Kang, C. W. Kim, A. U. Pawar, H. G. Cha, S. Ji, W.-B. Cai, Y. S. Kang, *ACS Energy Lett.* **2019**, *4*, 1549.
- [117] G. Bharath, K. Rambabu, A. Hai, N. Ponpandian, J. E. Schmidt, D. D. Dionysiou, M. A. Haija, F. Banat, *Appl. Catal., B* **2021**, *298*, 120520.
- [118] X. Wang, L. Lu, B. Wang, Z. Xu, Z. Xin, S. Yan, Z. Geng, Z. Zou, *Adv. Funct. Mater.* **2018**, *28*, 1804191.
- [119] R. Wang, X. Wang, W. Weng, Y. Yao, P. Kidkhunthod, C. Wang, Y. Hou, J. Guo, *Angew. Chem., Int. Ed.* **2022**, *61*, e202115503.
- [120] E. Barton Cole, P. S. Lakkaraju, D. M. Rampulla, A. J. Morris, E. Abelev, A. B. Bocarsly, *J. Am. Chem. Soc.* **2010**, *132*, 11539.
- [121] H. Ohtsu, K. Tanaka, *Angew. Chem., Int. Ed.* **2012**, *51*, 9792.
- [122] J. T. Muckerman, P. Achord, C. Creutz, D. E. Polyansky, E. Fujita, *Proc. Natl. Acad. Sci. USA* **2012**, *109*, 15657.
- [123] A. J. Morris, G. J. Meyer, E. Fujita, *Acc. Chem. Res.* **2009**, *42*, 1983.



**Shaohan Xu** received her master's degree in Chemical Engineering from Columbia University in 2020. She is currently a PhD candidate under the supervision of Prof. Guohua Zhao at School of Chemical Science and Engineering, Tongji University. Her research interests are energy and environmental photoelectrochemistry, focusing on electrochemical and photoelectrochemical CO<sub>2</sub> conversion and pollutants removal.



**Qi Shen** works in Institute of New Energy, School of Chemistry and Chemical Engineering, Shaoxing University. He received his Ph. D. in chemistry from the School of Chemical Science and Engineering under the guidance of Prof. Guohua Zhao. His current research interests include energy and environmental photoelectrochemistry, focus on the preparation of biophotovoltaic materials in CO<sub>2</sub> resource utilization for artificial photosynthesis.



**Jingui Zheng** received his master degree in material chemistry from the College of Chemistry and Material Science, Shandong Agricultural University in 2020. In the same year, he joined Tongji University, School of Chemical Science and Engineering, Shanghai Key Lab of Chemical Assessment and Sustainability, as a doctoral candidate under the guidance of Prof. Guohua Zhao. His current research interests are energy and environmental photoelectrochemistry, includes CO<sub>2</sub> conversion and pollutants removal.



**Nianjun Yang** is group leader of nanomaterials at the University of Siegen, Germany. He works on the growth and electrochemical applications of advanced carbon materials. He has published about 200 journal papers, edited 1 book series and 4 books, contributed 9 book chapters, organized 10 European Materials Research Society symposiums, and acted as the guest-editor of 10 journals such as *Accounts of Chemical Research*, *Small*, *Carbon*, *ACS Applied Materials and Interfaces*, *Nanoscale*. He is working as the associated editor of *Materials Lab*, editor board member of the journals of *Scientific Reports*, *Diamond and Related Materials*, *Nano Research Energy*, and *Materials Futures* as well as the program committee member of several diamond related international conferences.



**Guohua Zhao** is a professor at School of Chemical Science and Engineering, Tongji University, China, where he obtained his Ph.D. degree in Environmental Chemistry in 1999. After one year as a visiting fellow at University of Stuttgart, he joined the School of Chemical Science and Engineering, Tongji University. His current research interests include photoelectric catalysis and environmental energy chemistry, committed to cross field research work of environment and energy, such as CO<sub>2</sub> reduction, hydrogen production, photoelectrocatalytic oxidation and analysis of pollutants. Up to now, he has published 1 academic book and more than 190 research papers in peer-reviewed journals.